



Lithostratigraphy, Geochronology and Early Humans: The evolution of Quaternary volcanic successions and their impact on archaeological sites in the north-western edge of the Ararat Depression, Armenia

H. Gevorgyan ^{a,b,*}, T. Karampaglidis ^c, S. Nomade ^d, K. Fenn ^e, A. Petrosyan ^f, B. Gasparyan ^f, I.A.K. Oikonomou ^g, A. Malinsky-Buller ^g

^a TU Bergakademie Freiberg, Institute for Mineralogy, Brennhausgasse 14, 09599, Freiberg, Germany

^b Institute of Geological Sciences, National Academy of Sciences of the Republic of Armenia, Marshal Baghramyan Avenue, 0019 Yerevan, Armenia

^c Department of Geological and Mining Engineering, Castilla-La Mancha University, Toledo, Spain

^d LSCE, UMR 8212, CEA-CNRS et Université de Versailles St-Quentin and Paris-Saclay, 91198, Gif-sur-Yvette Cedex, France

^e Department of Geography and Planning, University of Liverpool, Liverpool, L69 7ZT, UK

^f Institute of Archaeology and Ethnography, National Academy of Sciences of the Republic of Armenia, Charents str. 15, 0025 Yerevan, Armenia

^g The Institute of Archaeology, Hebrew University, Jerusalem, Israel

ARTICLE INFO

Handling editor: Donatella Magri

Keywords:

Volcanic successions
Geochemistry
 $^{40}\text{Ar}/^{39}\text{Ar}$ dating
Ararat depression
Terraces formation
Lower Paleolithic

ABSTRACT

This paper explores the geological context of Dalarik-1 Cave, located in the Mastaraheghehat River Gorge within the Aragats Volcanic Province (AVP) in Armenia. By integrating lithostratigraphy, geochronology, and geomorphology, we examine the processes that shaped the cave and its associated terrace sequence, establishing chronological constraints on the cave's bedrock and its development within the broader fluvial landscape. Volcanic rocks in the studied area exhibit geochemical evidence suggesting a subduction-modified mantle source, potentially influenced by slab-derived fluids or melts. Geochronological data from $^{40}\text{Ar}/^{39}\text{Ar}$ dating indicate that volcanic activity in the study area occurred between approximately 900 and 660 ka, encompassing the first and second AVP eruption stages. The formation of the cave is linked to river incision that followed the deposition of the youngest volcanic unit of the local plateau, dated to 656.6 ± 40.0 ka. This incision is associated with the development of four fluvial terraces (T1 to T4), with the lower terraces (T3 and T4) dated between ~ 35 and 9 ka, reflecting intervals of climatic variability and/or tectonic activity. The cave is interpreted to have formed during a relatively stable phase of river activity, coinciding with the formation of the T2 terrace. It developed through both chemical and mechanical erosion within the volcanic bedrock. Based on these relationships, the formation of the cave likely occurred after the incision of the gorge ($post-656.6 \pm 40.0$ ka) and prior to the deposition of the T3 terrace, dated by optically stimulated luminescence (OSL) to 32.5 ± 2.3 ka. The cave site of Dalarik-1 contains Lower Paleolithic artifacts indicating human occupation after the cave's formation and provides rare insights into early human activities in the region. The study of the regional landscape evolution and the interplay between volcanic, fluvial, and climatic processes contributes to the broader understanding of the cave formation mechanisms in volcanic landscapes, offering valuable insights for future studies of Paleolithic sites in the Armenian Highlands.

1. Introduction

In recent decades, there has been a growing interest in understanding the interaction between physical landscapes and patterns of human evolution (Potts, 1996, 2013). This perspective conceptualises

archaeological sites as geomorphological phenomena, emphasizing the importance of natural processes in their formation and preservation (Dunnell, 1992; Foley, 1981a, 1981b). The preservation of hunter-gatherer activities over Pleistocene landscapes depends on rapid burial followed by stable sedimentary conditions that protect sites from

This article is part of a special issue entitled: Southern Caucasus published in Quaternary Science Reviews.

* Corresponding author. TU Bergakademie Freiberg, Institute for Mineralogy, Brennhausgasse 14, 09599, Freiberg, Germany.

E-mail addresses: Hripsime.Gevorgyan@mineral.tu-freiberg.de, hripsime.gevorgyan.geology@gmail.com (H. Gevorgyan).

<https://doi.org/10.1016/j.quascirev.2025.109623>

Received 14 July 2025; Received in revised form 9 September 2025; Accepted 12 September 2025

Available online 22 September 2025

0277-3791/© 2025 The Authors. Published by Elsevier Ltd. This is an open access article under the CC BY license (<http://creativecommons.org/licenses/by/4.0/>).

erosion. However, to be studied today, these sites must eventually be exposed from their initial burial context (Pope et al., 2016). While site formation processes are often examined at individual sites (Malinsky-Buller et al., 2011) or paleo-landscape levels (Bunn et al., 1980; Hovers et al., 2014; Oron et al., 2023), there has been limited focus on the broader-scale landscape formation processes—such as burial, stabilization, and subsequent exposure—that shape the regional distribution of Paleolithic remains.

The geological and geomorphological history of the Armenian Highlands and its Paleolithic record of the Quaternary period are significantly shaped by a volcanic activity (Ghukasyan, 1985; Meliksetian et al., 2014; Gevorgyan et al., 2020; Kirscher et al., 2020). The earliest evidence of hominin expansion outside Africa, dating to approximately 1.85–1.77 Ma, was discovered at the Dmanisi site in Georgia (Fig. 1a; Ferring et al., 2022, 2011), which is preserved within a volcanic landscape (Messager et al. 2010, 2011a,b; Nomade et al., 2016). Similarly, the Mid-Pleistocene site of Nor Geghi-1 in Armenia, embedded between two volcanic flows dated between 400–200 ka, illustrates the connection between volcanic dynamics and Lower Paleolithic sites (Fig. 1a; Adler et al., 2014; Sherriff et al., 2019, 2022). Armenian Highlands experienced continuous volcanic activity from the Pleistocene to the Holocene (Ghukasyan, 1985; Meliksetian et al., 2021; Neill et al., 2015; Sugden et al., 2021), with the AVP noted for its extensive and multi-phase volcanic activity spanning from 1.5 to 0.45 Ma (Gevorgyan et al., 2018, 2020).

Understanding the timing of human occupation within dynamic volcanic landscapes is not always straightforward, and usually two explanatory scenarios are proposed. According to the first scenario, volcanic eruptions buried earlier landscapes, subsequently exposed through river incision and erosion (Adler et al., 2014; Hay, 1976; Potts et al., 1999; Sherriff et al., 2019). Alternatively, rivers downcutting created terraced landscapes, which were later exploited by hunter-gatherers (Antoine, 1994; Antoine et al., 2000; Bridgland, 2000). Evaluating these scenarios is crucial for accurately positioning Paleolithic sites within their geological, geomorphological, and chronological contexts.

The Lower Paleolithic site of Dalarik-1 Cave is located within the AVP (Figs. 1 and 2). The site is situated on the banks of the

Mastarahegheghat River Gorge, flowing into the Ararat Depression (Fig. 2). The gorge exposes a range of volcanic materials, including basaltic to andesitic lava flows, pyroclastic flows, and fallout deposits (Gevorgyan et al., 2018, 2020; Meliksetian et al., 2014), some of which are outcropped along the southern reaches of the gorge (Fig. 2). The site provides a unique opportunity to test hypotheses about the landscape-scale formation processes.

The current paper provides the geological, geomorphological, and chronological frameworks for positioning these unique Lower Paleolithic assemblages within those two opposing depositional scenarios.

2. Geological and geographical overview

2.1. Geological settings

The present tectonic configuration of the Arabian-Eurasian collision zone reflects a complex geodynamic evolution from the Late Paleozoic to the Cenozoic, partially recorded in extensive tectono-stratigraphic terranes stretching from the Mediterranean to Tibet (Nikogosian et al., 2023 and references therein). It also resulted in the development of several sedimentary basins oriented parallel to the uplifted Greater Caucasus Mountain belt and Armenian Highlands.

These include the Rioni and Kura Basins to the north and the Mid-Araxes Basin to the south, encompassing the Nakhichevan and Ararat depressions (Gabrielyan et al., 1981; Philip et al., 1989). The Ararat Depression, a Cenozoic pull-apart basin, spanning approximately 100 km in a NW-SE direction with a variable width of 20–45 km, has a complex geological history driven by Neogene-Quaternary tectonic, volcanic, and sedimentary processes (Rebai et al., 1993; Philip et al., 2001; Karakhanian et al., 2003; Avagyan et al., 2018). The Ararat Depression, positioned at the north-eastern part of the Armenian Highlands, is bordered by major active faults, including the Garni and Doğubayazit faults, and is flanked by the Aragats and Gegham volcanic complexes to the north and the Ararat volcano high to the south, reflecting Armenia's neotectonic framework of active strike-slip fault zones (Karakhanian et al., 2016; Avagyan et al., 2018). The surrounding volcanic complexes, dating from the Upper Pliocene to the Quaternary period (Innocenti et al., 1982; Pearce et al., 1990; Karapetian et al.,

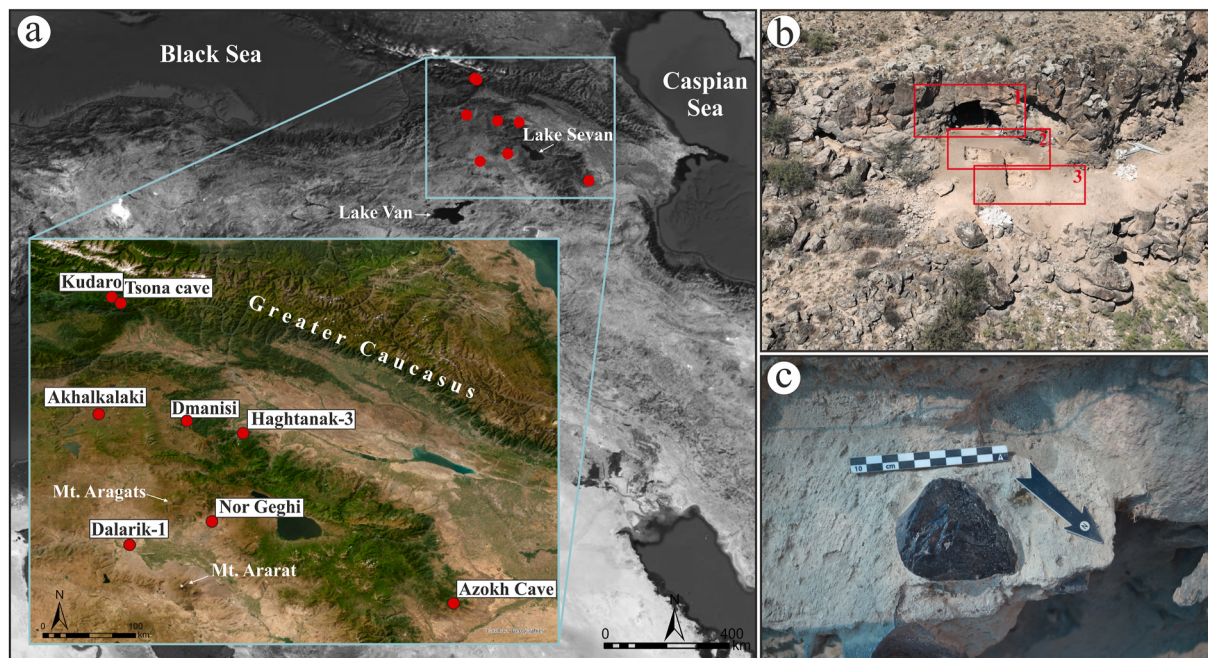


Fig. 1. a) The locations of the Early and Middle Pleistocene sites in the Southern Caucasus and Armenian Highlands, b) Aerial view of Dalarik-1 Cave and the different excavation areas: 1. internal part of the cave, 2. entrance of the cave, 3. external part of the cave. c) An obsidian bifacial tool as found during the excavation.

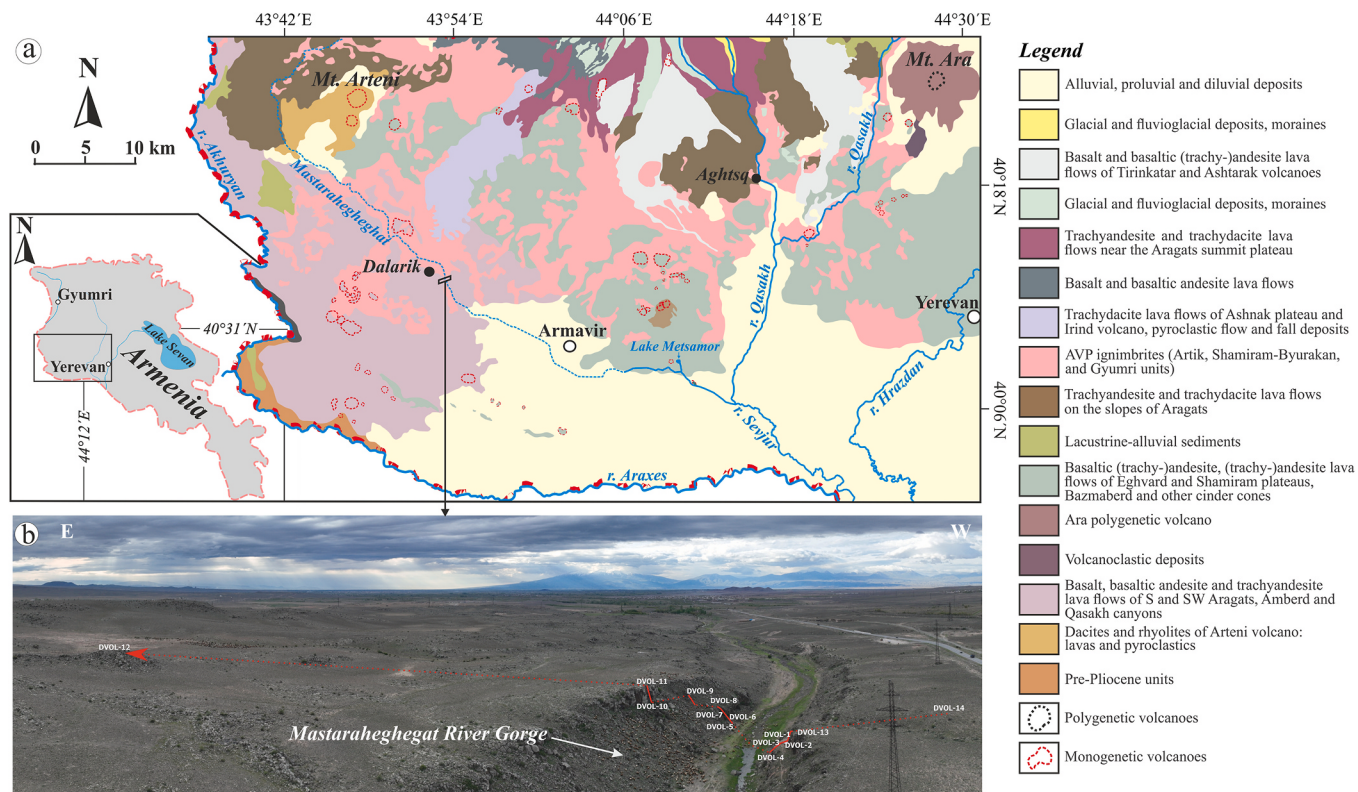


Fig. 2. a) Geological map of the southern part of the Aragats Volcanic Province, Armenia (modified after Gevorgyan et al., 2020). b) Aerial view of basaltic (trachy-) andesite and trachyandesite lava flows outcropping along both sides of the southernmost reaches of the Mastarahegheghat River Gorge, Armenia.

2001; Chernyshev et al., 2002; Lebedev et al., 2011; Meliksetian et al., 2014; Gevorgyan et al., 2018, 2020; Kirscher et al., 2020), and high neotectonic activity (Karakhanian et al., 2004, 2016; Avagyan et al., 2018) have resulted in significant sediment accumulation (up to 250 m) and pronounced topographic heterogeneity (Karakhanian et al., 2003; Sayadyan, 2009; Avagyan et al., 2018). Finally, the Ararat Depression is transacted by the Araxes River, dividing the depression between Armenia in the north and Turkey and Iran in the south (Sayadyan, 2009; Avagyan et al., 2018). From a paleoenvironmental perspective, research conducted in the area has revealed a region characterized by diverse landscapes and biotopes (Nakhtsrishvili, 2012; Fayvush and Aleksanyan, 2016). Analysis of lake deposits, alluvial sediments, glacier evolution, and Paleolithic sites has provided insights into the region's environmental responses to global climate changes (Djamali et al., 2008; Joannin et al., 2014; Pickarski et al., 2015; Chahoud et al., 2016; Pickarski and Litt, 2017; Malinsky-Buller et al., 2020; Sherriff et al., 2022; Oikonomou et al., 2025; Carrasco et al., 2025; Karampaglidis et al., 2025).

Although previous investigations have addressed the tectonostratigraphic framework and the paleoenvironmental context of the Ararat Depression, as well as hominin activity at Dalarik-1 (Avagyan et al., 2018; Gasparyan et al., 2023), there is still a significant gap in understanding the geological and geomorphological evolution of the Mastarahegheghat River Gorge. This study presents the results of field mapping, alongside petrographic, petrologic, geochemical, and geochronological analyses, to understand the volcanic history of the region and the subsequent geomorphic processes that formed the Mastarahegheghat River Gorge.

2.2. The Mastarahegheghat River drainage basin

The Mastarahegheghat River is over 100 km long, with its source located west of Mount Aragats at an altitude of ca. 2500 m a.s.l.

(Geology of the Armenian SSR, 1962). The river subsequently flows around Mount Arteni (2047 m a.s.l.), traversing part of the Talin-Karmrashen Plateau before ultimately flowing into the Ararat Depression, where it connects with the Sevjur River (Fig. 2a). The initial 40-km segment of the river's trajectory exhibits a north-easterly to south-westerly orientation, subsequently undergoing a pronounced change in direction, veering from north-west to south-east, aligning with the Araxes River (Fig. 2a). The river's course is characterized by the cutting of volcanic rocks of intermediate to mafic composition, with a predominant origin from the magmatism of the Aragats stratovolcano and monogenetic volcanoes from AVP, spanning an age range from the Lower Pleistocene to the Middle Pleistocene (Arakelyan, 1949; Geology of the Armenian SSR, 1962, Geology of the Armenian SSR, 1964; Innocenti et al., 1982; Pearce et al., 1990; Karapetian et al., 2001; Chernyshev et al., 2002; Lebedev et al., 2011; Gevorgyan et al., 2020, 2018; Glauberman et al., 2020). The Mastarahegheghat River exemplifies a typical bedrock river in a highly dynamic tectonic, volcanic and climatically active mountainous region (Arakelyan, 1949; Gabrielyan et al., 1981; Innocenti et al., 1982; Philip et al., 1989; Avagyan et al., 2018; Gevorgyan et al., 2020; Carrasco et al., 2025).

2.3. The Lower Paleolithic site of Dalarik-1

The Lower Paleolithic site of Dalarik-1 ($40^{\circ}13'8.8''N$, $43^{\circ}53'38.0''E$, 930 m a.s.l.) is embedded in both a small cavern with an approximate area of $19 m^2$, as well as the outside surface exposed over an area of $50 m^2$ on a +11m terrace above the current riverbed. It features a main linear corridor measuring 7.6 m in length, 3.8 m in width, and 2.3 m in height (Fig. 1b, 5 and 6). The site was initially excavated by an Armenian-Japanese team, revealing a lithic assemblage dominated by diagnostic Lower Paleolithic artifacts, primarily manufactured from obsidian, with a smaller number produced on dacite (see Gasparyan et al., 2023: Figs. 8, 11–13; and Fig. 3: I, II, VI, this paper). In addition, a



Fig. 3. I, II and VI: Obsidian bifacial tools made on large flakes; III and V: Transversal scrapers made with Quina retouch.

few fossilized faunal remains were found, including fragments of large mammal bones, possibly horse taxa. Our research group conducted two additional seasons in 2022–2023. In total, 24 m² has been excavated so far, and a 7-m longitudinal section was established along the inner part of the cavern to the front slope of the terrace. Eight main sedimentological units were observed and sampled for sedimentology and dating in the external part of the cave, while another five sedimentological units were found in the cave. Currently, the stratigraphic correlation between the cave interior and exterior is under investigation. Five sedimentological units in the exterior and interior contained lithic and faunal assemblages. The lithic assemblage retrieved comprised ca. 1500 obsidian and ca. 80 dacite artifacts. In both raw materials, the frequency of retouched pieces is very high, with no evidence of on-site production but mainly use and rejuvenation. Among the represented retouched pieces in both raw materials, bifacial tools dominate the assemblages, mostly made on large flakes. Among the unifocal tools, there is a high frequency of scrapers with stepped (Quina) retouch on various typologies such as side and transverse scrapers (Fig. 3: III, V; Bar-Yosef, 1994; Adler et al., 2014).

3. Sampling and analytical methods

Eight geological-archaeological sections and a schematic cross-section geological-geomorphological profile through the Mastaraheghehat River Gorge were logged. The variable lava flows, pyroclastic flow, and fall deposits were characterised and traced, documenting lateral facies variations. The studied units were described in terms of their textural and structural features, including variations in lithic and mineral composition and the degree of weathering, at each outcrop. GPS data for the key stratigraphic sections are provided in *Supplementary Table 1*.

The thematic mapping (Fig. 5) was conducted using a range of remote-sensed data, including: (i) 15 m Terra colour imagery for small and mid-scale analysis, 2.5 m SPOT imagery, and the Vivid Advanced imagery base map, which includes the first 30 cm high-definition (HD) satellite imagery base map, (ii) 1:500,000-scale geological maps from the Geological Service of the Republic of Armenia, (iii) topographic maps from open sources, and (iv) Digital Elevation Models (DEM) with a 5 m resolution. Mapping was performed at a 1:25,000 scale using the WGS 1984 coordinate system. The mapping process was supported by field analysis of Quaternary landforms and sedimentary structures to develop the stratigraphy of Quaternary deposits.

To create the geomorphological maps, first, photointerpretation was carried out (see *Supplementary Fig. 1*). The resulting maps were then digitized onto orthoimages and shaded relief models derived from DEMs with a 5m pixel resolution. These models were instrumental in accurately delineating the distribution of key cartographic features. The digitization was performed using ArcGIS V.10.8.1 software. The preliminary maps were further refined through field mapping, sedimentary analysis, and stratigraphic detailing. Specific locations were recorded using a handheld GPS device, which provided an accuracy of 3–5 m.

Petrographic studies were conducted on 16 polished thin sections at the Institute of Mineralogy, TU Bergakademie Freiberg (TUBAF), Germany. The mineralogical composition and texture of the rocks were examined using Axio Lab. A1 polarization microscopy at magnifications of 5× and 10x in both plain polarised light (PPL) and crossed polarised light (XPL). Additionally, a digital microscope was employed to enhance the visualisation of internal and external texture variations of the primary mineral components. Thin-section scans and mineral photographs were captured with a Keyence VHX-5000 digital microscope at the Institute of Geology (TUBAF, Germany). Preliminary qualitative and semi-quantitative compositional analyses, including combined energy-dispersive X-ray spectroscopy (EDS) and backscattered electron (BSE) imaging, were performed using the FEI QUANTA 600F scanning electron microscope at the Institute for Mineralogy (TUBAF, Germany) to identify the mineral phases and their zonation patterns. The operating

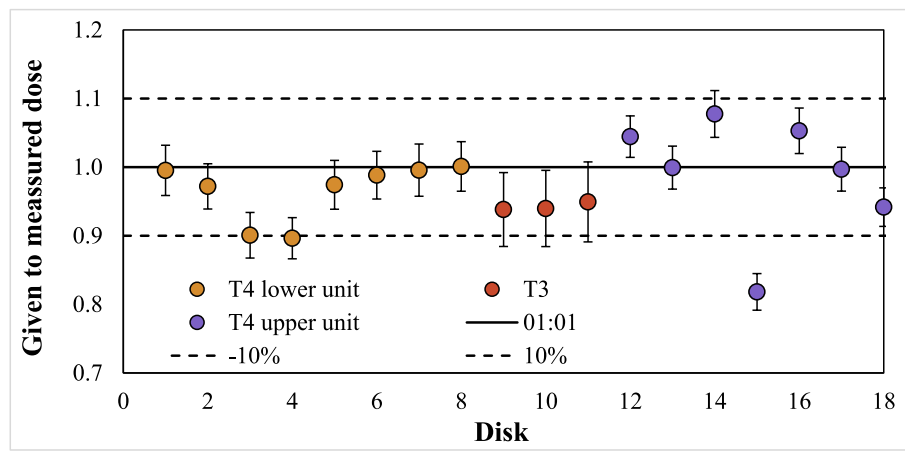


Fig. 4. Dose recovery results for three OSL samples investigated in this study.

conditions were set to a 25 kV acceleration voltage, 10 nA beam current, and a 12 mm working distance.

The chemical composition of 16 representative whole-rock samples was analysed at ALS Minerals in Dublin, Ireland. Major oxides and base metals were determined using inductively coupled plasma-atomic emission spectrometry (ICP-AES), while trace and rare earth elements were analysed by inductively coupled plasma mass spectrometry (ICP-MS; blanks, standards and detection limits are presented in Supplementary Table 2).

Additionally, the overlying and underlying units were sampled to aid in stratigraphic correlation and age estimation. Two dating techniques were utilised: $^{40}\text{Ar}/^{39}\text{Ar}$ step heating method for dating lava flows and the Optically Stimulated Luminescence (OSL) for dating sedimentary features. $^{40}\text{Ar}/^{39}\text{Ar}$ dating was conducted at the Laboratoire des Sciences du Climat et de l'Environnement (CNRS-LSCE; Gif-Sur-Yvette, France), while OSL dating was undertaken at the Liverpool Luminescence Laboratory at the University of Liverpool, UK.

3.1. $^{40}\text{Ar}/^{39}\text{Ar}$ dating

Sample preparation: The procedure for preparing pure splits of groundmass is detailed in Guillou et al. (1996).

Mass spectrometric measurements VG 5400 (DVOL 2 and DVOL 4): Splits of 120–130 mg of groundmass and feldspars were wrapped into 99.5 % copper foil packets, loaded in aluminium disks and then irradiated in the CLICIT facility at the Oregon State University TRIGA reactor for 120 min (CO#018). Neutron fluence (J) was monitored by co-irradiation of ACs crystals (Nomade et al., 2005) placed in three pits encircling each sample. The J value for each sample was usually determined from 5 to 6 single-crystal laser fusion analyses of ACs and is reported in the supplementary tables along with the correction factors for interfering neutron reactions. Corresponding J values were calculated using an age of 1.1891 ± 0.0008 Ma (Niespolo et al., 2017). The total decay constants of Renne et al. (2011) and the $^{40}\text{Ar}/^{36}\text{Ar}$ atmospheric ratio at 298.56 (Lee et al., 2006) were used for age calculations. After irradiation, samples were loaded into a stainless-steel carousel over a double-vacuum resistance furnace and degassed at 550–600 °C to remove unwanted large quantities of atmospheric argon. Extraction and gas clean-up procedures followed during the step-heating experiments, as well as the mass-spectrometric experiments, were identical to the ones detailed in Guillou et al. (2011). Pure groundmass aliquots were incrementally heated in 10–11 steps between 600° and 1200 °C using the double-vacuum resistance furnace. Isotopic measurements were achieved using a high-sensitivity noble gas GV5400 instrument operated in ion counting mode. One analytical run consists of 20 peak scans of each argon isotope with integration times of 2 s (^{40}Ar , ^{39}Ar), 10 s (^{37}Ar , ^{38}Ar , baseline) and 20 s (^{36}Ar), first preceded by a peak centring routine

on the five Ar isotopes, upon admission of the sample into the mass-spectrometer. Raw argon isotope abundances are regressed back to inlet time using ArArCalc software (Koppers, 2002) based on a linear or polynomial least-squares fit. The instrument atmospheric calibration is performed using a dedicated air-calibration system featuring a 6-L tank filled with purified atmospheric argon and made over a wide dynamic range with a precision better than 0.15 % (2σ ; standard deviation for multiples of experiments) for any given beam size measured. System blanks were measured prior to step-heating experiments at temperatures between 600 and 1300 °C. Blanks ranged from 3.0×10^{-16} and 2.2×10^{-15} mol of ^{40}Ar and from 1.4×10^{-18} and 7.8×10^{-18} mol of ^{36}Ar . These values are about 20–100 times smaller than the sample signals.

Mass spectrometric measurements NGX 600 (DVOL 5 and DVOL 10): A split of 20 mg of groundmass was point in one single hole within an aluminium disk and then irradiated in the CLICIT facility at the Oregon State University TRIGA reactor for 60 min (CO#023). Neutron fluence (J) was monitored by co-irradiation of ACs crystals (Nomade et al., 2005) placed in three pits encircling the sample. The J value was determined using 6 single-crystal laser fusion analyses of ACs and is reported in the supplementary tables along with the correction factors for interfering neutron reactions. Corresponding J values were calculated using an age of 1.1891 ± 0.0008 Ma (Niespolo et al., 2017). The total decay constants of Renne et al. (2011) and the $^{40}\text{Ar}/^{36}\text{Ar}$ atmospheric ratio at 298.56 (Lee et al., 2006) were used for age calculations. After irradiation, about 2 mg of groundmass was loaded in three adjacent pits within a copper 133 pits sample holder placed into a differential vacuum Teledyne Cetac window connected to a home-designed compact extraction line. The three pits with the groundmass were step-heated at the same time using a 100 W Teledyne Cetac CO₂ laser during a total of 180 s between 0.35 and 2.8 W (9 steps). Before the step-heating experiment, each groundmass pit underwent a 60s long sweeping at 0.3 W to remove unwanted gas potentially trapped on the surface and fractures. Extracted gases were first purified by a SAES GP 50 cold getter for 500s and then for 500s by two hot SAES GP 50 getters. The five Argon isotopes (i.e., ^{40}Ar , ^{39}Ar , ^{38}Ar , ^{37}Ar and ^{36}Ar) were measured using a multicollector NGX 600 mass spectrometer equipped with 9 ATONA® amplifiers array and an electron multiplier. More technical specifications regarding the NGX 600 ATONA detector array are presented in detail in Cox et al. (2020). ^{40}Ar , ^{39}Ar , ^{38}Ar , and ^{36}Ar isotopes were collected simultaneously while the ^{37}Ar was measured in a second time. In the first run, ^{40}Ar , ^{39}Ar and ^{38}Ar were measured simultaneously on 3 ATONA® amplifiers and ^{36}Ar on the electron multiplier. Following this first run, the ^{37}Ar was measured alone using the electron multiplier. Each isotope measurement corresponds to 20 cycles of 20-s integration time. Peak intensity data were reduced using ArArCALC V2.4 (Koppers, 2002). To verify the detectors' linearity, mass discrimination was monitored by analysis of at least 40 air shots of

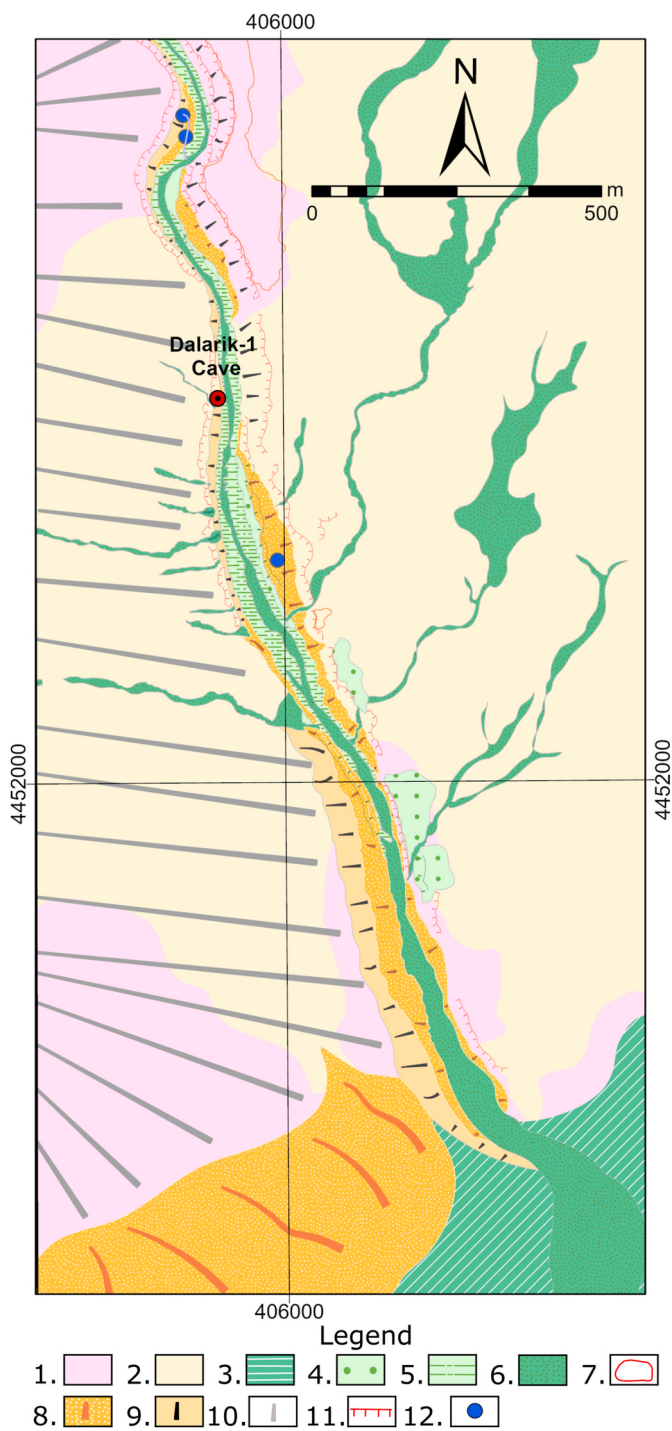


Fig. 5. Detailed geomorphological map of the study area. Legend: 1. Pyroclastic flow and fallout deposits (Quaternary), 2. Basaltic (trachy-) andesites and trachyandesites, 3. Quaternary infill of the Ararat Depression, 4. Strath terraces, 5. Floodplain, 6. Alluvial deposits, 7. Strath surface, 8) Debris flow, 9) Debris talus, 10) Glacis, 11) Scarp, 12) OSL samples.

various ion beam intensities, ranging from 6.0×10^{-2} to 4.0×10^{-2} V (1–4 air shots). About 15 air shot analyses are performed every day. These measurements are done automatically during the nights before and after the unknown measurements. Procedural blank measurements were achieved after every two steps (see Supplementary Table 3).

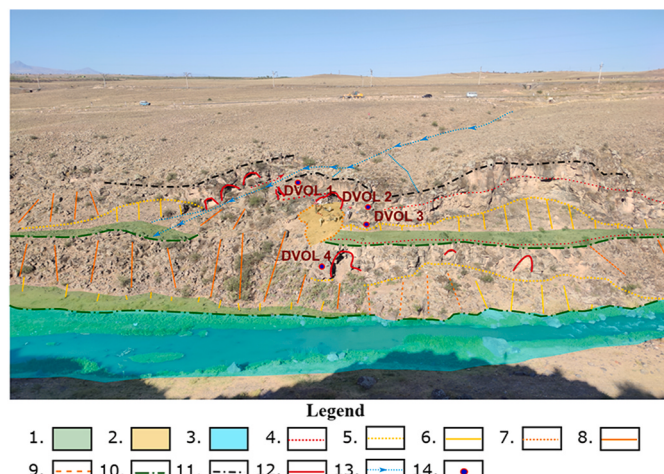


Fig. 6. Aerial view of the Dalarik-1 Cave. Legend: 1. Strath terrace levels and surfaces, 2. Excavation area, 3. Floodplain, 4. Contacts between the lithologic units of the bedrock, 5. Contacts of the debris deposits, 6. Debris talus matrix-supported, 7. Limits of the excavation area, 8. Debris talus clast-supported, 9. Erosive glacis, 10. Fluvial scarp, 11. Scarp, 12. Karstic features, 13. Hydrographic net, 14. Sample logs.

3.2. Optically stimulated luminescence

Luminescence samples were collected by hammering opaque tubes into freshly cleaned exposures, avoiding large rock pieces where possible. Samples were prepared and measured at the Liverpool University luminescence laboratory under subdued lighting conditions. The light-exposed ends of the sampling tube were removed and retained for the water content and dosimetry measurements.

The sediment was first treated with 37 % HCl to remove carbonates and 20 % H₂O₂ to remove organic matter. Following chemical treatment, samples were sieved to remove >63 µm fractions. The remaining fine sediment was settled using Stokes' equation to isolate the 4–11 µm fraction. Aliquots for analysis were made by dispensing a fine-grain polymimetic fraction onto the surface of 9.8 mm aluminium discs.

Equivalent dose (De): All luminescence measurements were performed using an automated Risø TL/OSL DA-15 system equipped with a ⁹⁰Sr/⁹⁰Y beta source (Bøtter-Jensen et al., 2003) fitted with a blue filter pack (BG39, Coring 7–59) in front of the photomultiplier tube. Standard single-aliquot regenerative dose (SAR) protocols were used for the analyses (Murray and Wintle, 2000). A preheat of 250 °C for 60s was applied before stimulations at 225 °C for 200s IR LEDs. An elevated temperature (290 °C) IR LEDs bleach off for 300s was also added to the end of each Lx/Tx cycle. The signal from the first 1s of stimulation was integrated, while the background was calculated by integrating the final 100s. Standard rejection criteria were used to screen data and account for the associated uncertainties: (1) test dose response >3σ above the background; (2) test dose uncertainty <20 %, (3) recycling ratio found within 1 ± 0.1 ; and (4) recuperation <5 % of the response from the largest regenerative dose. De values were calculated from all aliquots that passed rejection criteria.

The performance of the pIRIR₂₂₅ protocol was assessed using a dose recovery test on all samples (Fig. 4). The average dose-to-measured ratio for three samples is 0.97 ± 0.04 . The respective ratios for T4 lower unit, T3, and T4 upper unit are 0.97 ± 0.03 , 0.94 ± 0.06 , and 0.99 ± 0.03 . Fading rates (g-values, Aitken, 1985) were measured for the same samples used for dose recovery. Each value was determined for four aliquots and normalized to a tc of two days (Huntley and Lamothe, 2001). The average IR₅₀ fading rates are at 4.8 ± 1.35 %/decade and at -4.28 ± 3.06 %/decade for pIRIR₂₂₅ signals, which show no need for applying fading correction to pIRIR₂₂₅ signals in line with previous studies. In all age determinations, the central age model (CAM) was

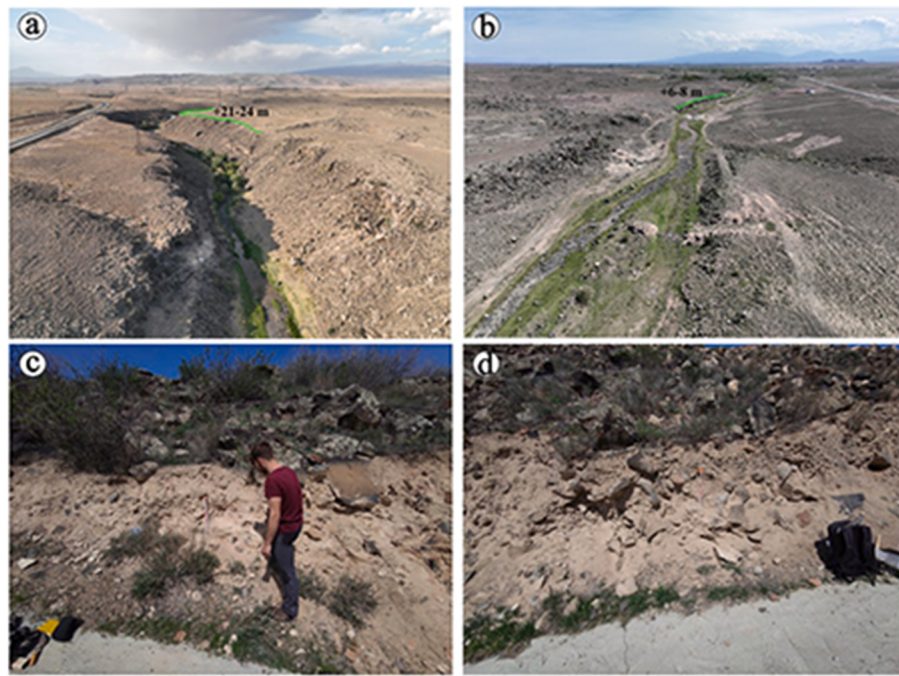


Fig. 7. a) Aerial view of the east part of the gorge of the Mastarahegheghat River and +21–24 m terrace. b) Aerial view of the eastern gorge opening of the Mastarahegheghat River and +6–8 m terrace. c) Sedimentary section of the +6–8 m terrace. d) Sedimentary section of the +3–5 m terrace.

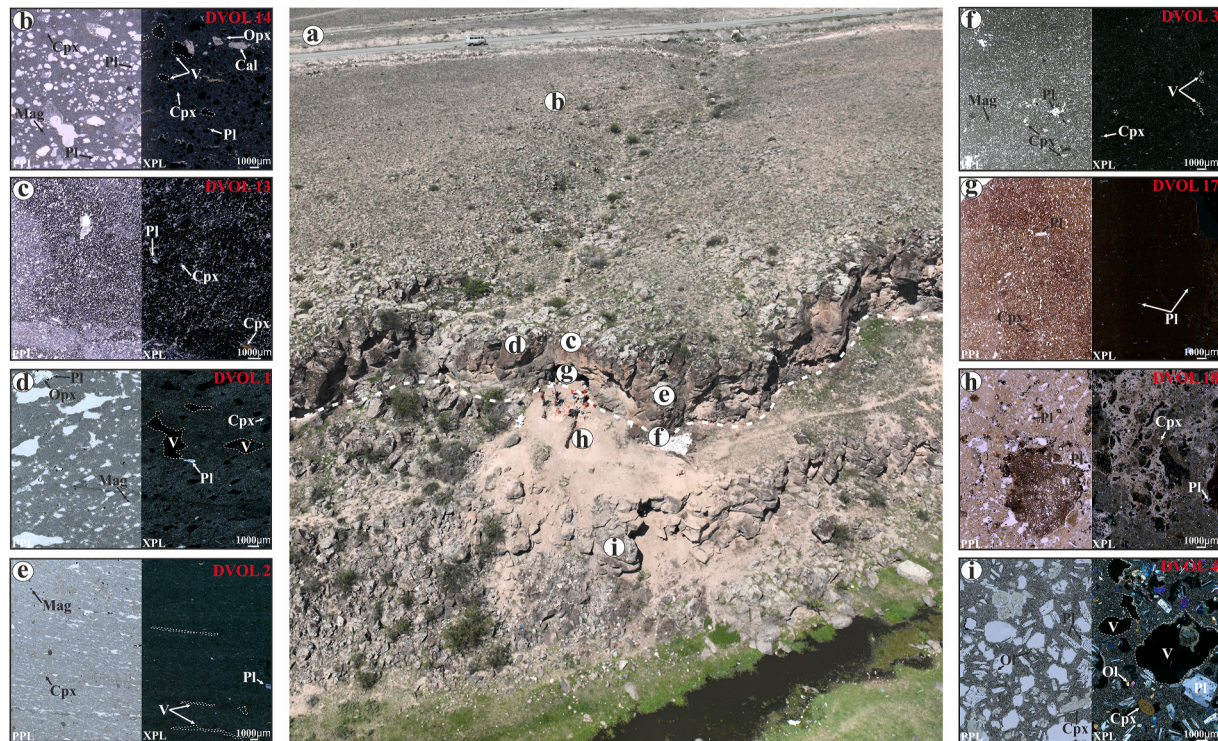


Fig. 8. a) Photograph of the outcrop showing the lava flows exposed on the right bank of the Mastarahegheghat River Gorge, with sampling points marked and a dashed line indicating the assumed boundary zone between the lava flows. b-i) Photomicrographs of thin sections under plane-polarized light (PPL) and cross-polarized light (XPL), highlighting the textural and mineralogical variations in the studied lava flows: b) Photomicrographs of thin section DVOL 14, exhibiting vesicular and locally amygdaloidal textures, along with porphyritic texture, and a low crystal content represented by plagioclase, clinopyroxene, orthopyroxene, and magnetite; c-f) Photomicrographs of thin sections DVOL 13, DVOL 1, DVOL 2 and DVOL 3, showing similar mineral assemblages and textural variations, with a gradual decrease in vesicular texture observed in DVOL 3; g) Photomicrographs of thin section DVOL 17, a basal breccia displaying low crystal content primarily consisting of plagioclase and clinopyroxene, with porphyritic texture. h) Photomicrographs of thin section DVOL 18, polymictic weathered material (archaeological site); g) Photomicrographs of thin section DVOL 4, crystal-rich lava with vesicular and porphyritic-globular textures, predominantly comprised of plagioclase, clinopyroxene, and olivine. Mineral abbreviations are after Whitney and Evans (2010): Cal – calcite, Cpx – clinopyroxene, Mag – magnetite, Ol – olivine, Opx – orthopyroxene, Pl – plagioclase; V – vesicle.

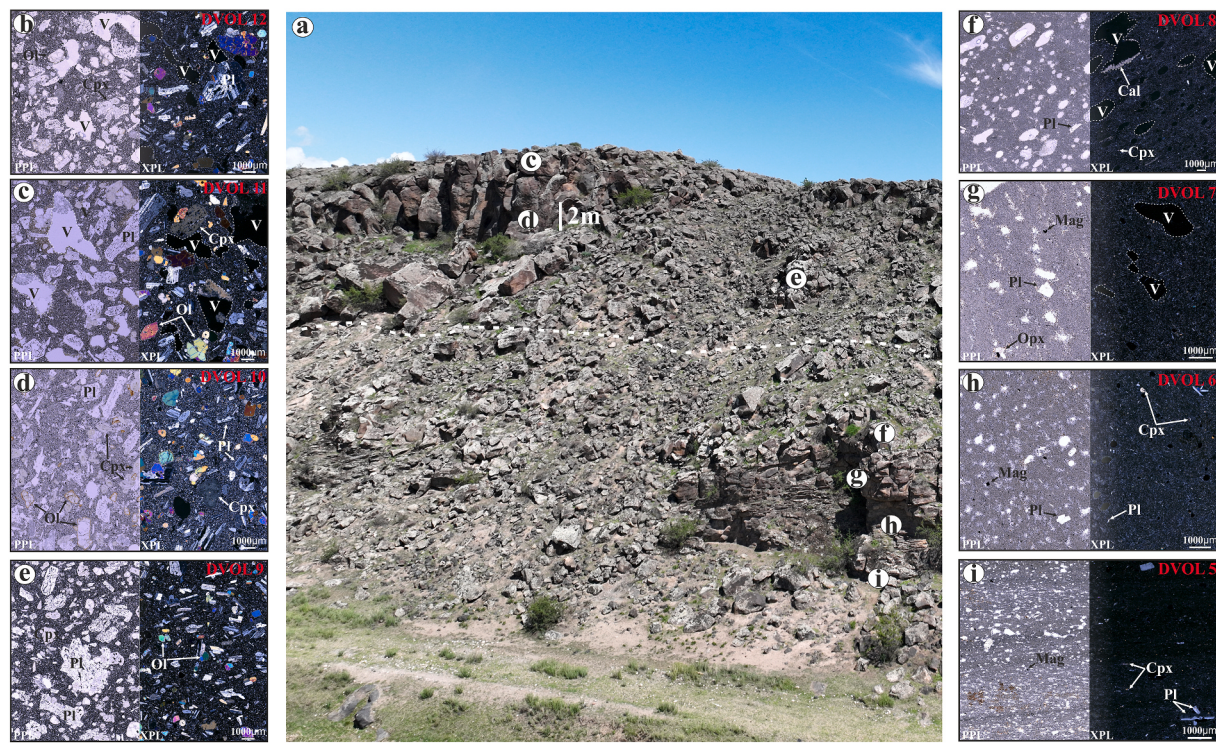


Fig. 9. a) Photograph of the outcrop showing the lava flows exposed on the left bank of the Mastarahegheghat River Gorge, with sampling points marked and a dashed line indicating the assumed boundary zone between the lava flows. b-i) Photomicrographs of thin sections under plane-polarized light (PPL) and cross-polarized light (XPL), highlighting the textural and mineralogical variations in the studied lava flows: b) Photomicrographs of thin section DVOL 12 (sampled 260 m to the NE of DVOL 11), exhibiting vesicular and locally amygdaloidal textures, along with porphyritic and glomerophytic textures, and a high concentration of idiomorphic to xenomorphic crystals of plagioclase, clinopyroxene, and olivine; c-e) Photomicrographs of thin sections DVOL 11, DVOL 10, and DVOL 9, showing similar mineral assemblages and textural variations, with a gradual decrease in vesicular texture observed in DVOL 9; f-i) Photomicrographs of thin sections DVOL 8, DVOL 7, DVOL 6, and DVOL 5, displaying low crystal content primarily consisting of plagioclase, clinopyroxene, orthopyroxene, and magnetite, with porphyritic and glomerophytic textures. Vesicular texture is present (partially filled by secondary minerals such as calcite), and the vesicle/porosity content increases from DVOL 5 to DVOL 8, toward the top of the lava flow.

applied as all samples had symmetrical De distributions.

Environmental dose-rate: Dose rates were measured using the μ Dose system (Kolb et al., 2022; Tudyka et al., 2020). For each sample, 2 g of milled material was placed under a dual-layer scintillator and the photomultiplier, and measured continuously for 48 h. Environmental dose rates were calculated in the μ Rate software (Tudyka et al., 2023) using the conversion factors of Cresswell et al. (2018) adjusted for grain size (alpha (Brennan et al., 1991) and beta (Guérin et al., 2011), and a moisture content of $7 \pm 5\%$ (estimated considering the field water contents and the environmental history for each sample), and cosmic dose (Prescott and Hutton, 1994), and an a-value of 0.11 ± 0.02 (Kreutzer et al., 2014).

4. Results

4.1. Detailed geomorphology of the study area

The Mastarahegheghat River at the study area flows directly over volcanic bedrock, with minimal coverage of very coarse sediment. Morphologically, the river exhibits irregular meanders with moderate sinuosity, characterized by single-phase meanders that widen at bends and are accompanied by point bars. The primary morphological features of the river valley include incised valleys with V-shaped gorges, narrow and confined channels bounded by steep valley walls, limited floodplain development, irregular channel beds, and high-gradient zones. Knickpoints are common and correspond to lithostructural transitions, typically marking shifts between more resistant lithologies, such as andesite and basalt, and less resistant materials, including thin alluvial deposits at the Ararat Depression, Kars Plateau, and volcanic scoria near Karakert

village. These knickpoints also align with broader geological transitions, such as those between the uplifted volcanic mountains (e.g., Mt. Aragats) and the Ararat Depression. Field observations highlight dominant erosion processes, including significant abrasion of the bedrock surface, plucking along pre-existing fractures, chemical weathering, and limited karstification (Figs. 1, 2, 5 and 6).

Sediment transport is constrained by minimal storage, a lack of extensive alluvial deposits, and the predominance of coarse detrital material, consistent with the behavior of bedrock rivers flowing over a hard-volcanic substrate with coarse bedload (Montgomery, 2004; Schanz and Montgomery, 2016; Karampaglidis et al., 2020). Within the study area, a sequence of five strath terrace levels and surfaces was identified: the floodplain, +3–5 m, +6–8 m, +11 m, and +21–24 m (Fig. 6).

Floodplain: Deposits are formed during overbank flooding events and consist of a 1-m-thick massive structure with moderate sorting. The sediments are primarily sands, silts, and clays, rich in organic matter and affected by root bioturbation.

+3–5 m Terrace: This terrace consists of a thin sediment layer (1–3 m) overlying bedrock. Two units were identified: (i) The lower unit is a poorly sorted, clast-supported deposit with sub-rounded, polymictic clasts (25–35 cm), imbricated and embedded in a silty-clay matrix, indicative of high-energy flow events. (ii) The upper unit is also clast-supported but moderately sorted, with rounded pebbles and clasts, and capped by debris talus formed from cliff face rockfall or debris flows. The upper unit has been dated to 9.3 ± 0.6 ka (OSL), and the lower unit to 14.8 ± 1 ka (OSL; Fig. 7d).

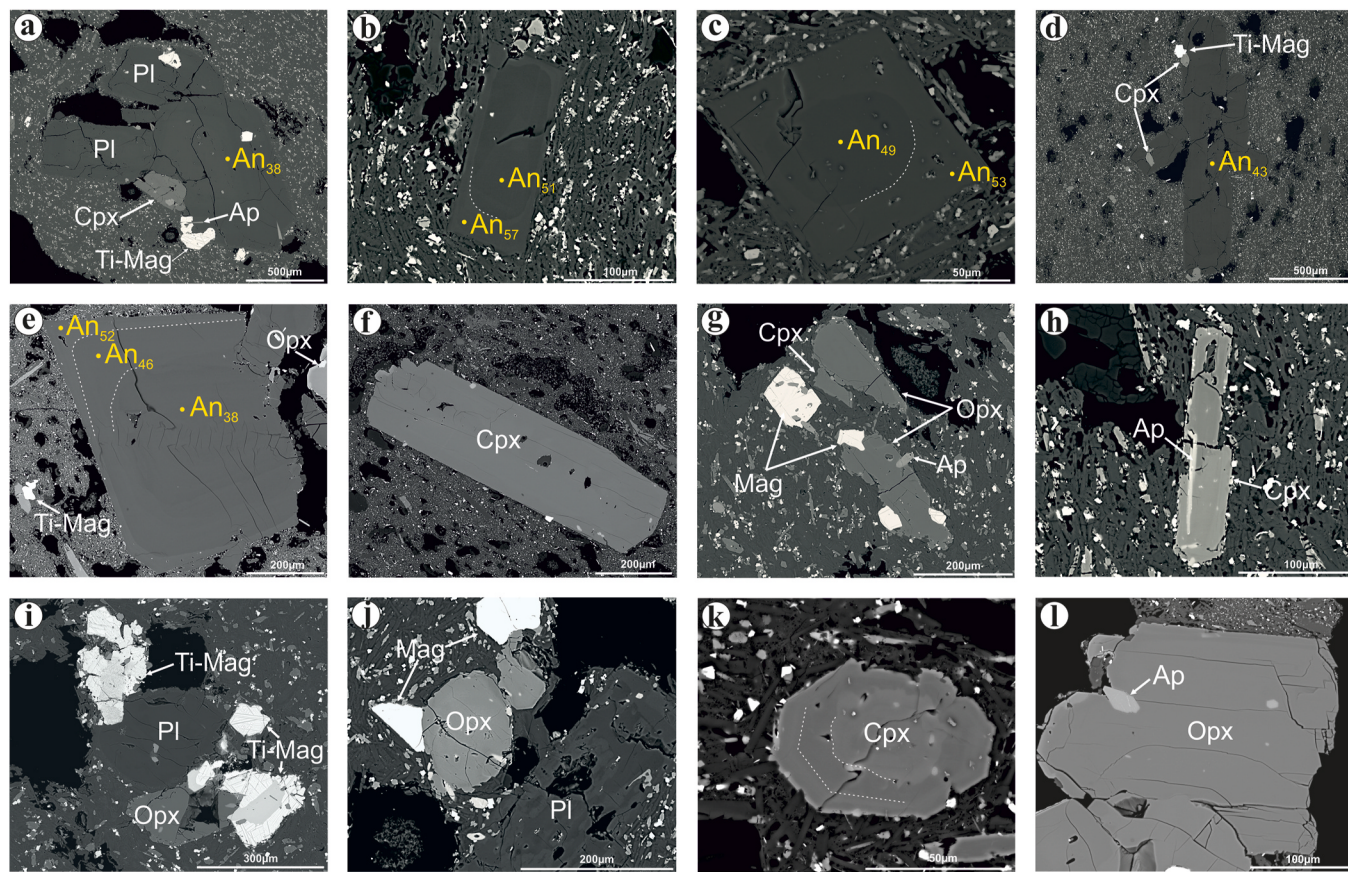


Fig. 10. BSE images of the main mineral phases from the crystal-poor lavas exposed on both the left and right banks of the Mastaraheghehat River Gorge: a) Glomerophytic aggregate of plagioclase and clinopyroxene with inclusions of titanomagnetite (with sandwich microtexture) and apatite needles (DVOL 1); b-c) Slightly reverse-zoned crystals of plagioclase (DVOL 2 and 3, respectively); d) Glomerophytic plagioclase with clinopyroxene and titanomagnetite inclusions (DVOL 5); e) Reverse-zoned subhedral plagioclase crystal (DVOL 14); f) Subhedral clinopyroxene crystal with a slightly resorbed core (DVOL 13); g) Ortho- and clinopyroxene crystals with magnetite and apatite inclusions (DVOL 1); h) Slightly zoned phenocryst of clinopyroxene with the inclusion of needle-like apatite (DVOL 2); i) Aggregate of plagioclase, orthopyroxene and zoned titanomagnetite (DVOL 14); j) Zoned plagioclase with coarse-sieve core and crystals of orthopyroxene and magnetite in microcrystalline groundmass (DVOL 14); k) Oscillatory-zoned clinopyroxene with apatite inclusions (DVOL 3); l) Glomerophytic orthopyroxene with the apatite inclusion (DVOL 13). Abbreviations: An – anorthite, Ap - apatite, Ti-Mag – titanomagnetite. For additional abbreviations, refer to the figure caption of Fig. 8.

+6–8 m Terrace: This terrace is exposed within the gorge (Fig. 5) and constitutes a thin strath terrace layer (0.5–1 m thick) with characteristics similar to the lower unit of the +3–5 m terrace. A poorly sorted, clast-supported deposit with sub-rounded, polymictic clasts, imbricated and embedded in a silty-clay matrix is dated to 32.5 ± 2.3 ka (OSL, Table 1). It is capped by debris talus (Fig. 7b and c). In contrast, at the gorge's (western) eastern opening into the Ararat Depression, the terrace appears as a strath surface with a thin alluvial cover of rounded, polymictic clasts.

+11 m Terrace: This layer is located near the entrance of the Dalarik-1 Cave. The formation of Dalarik-1 Cave is attributed to the interaction of surface and subsurface fluvial processes of the Mastaraheghehat River acting on basaltic and andesitic lava flows. The cave exhibits features that were shaped by both chemical dissolution and mechanical erosion resulting from flowing water. The lithological substrate of Dalarik-1 Cave consists of a dense, massive porous basaltic trachyandesite in the lower section, overlain by trachyandesite exhibiting bedding planes formed by successive lava flows. Intercalated between these flows are reddish, weathered volcanic breccias. Above these units lies a massive, dense, variably porous basaltic andesite. The cavity was primarily formed within the intermediate unit; a feature common to most karst elements observed in the valley within the study area. Morphologically, Dalarik-1 Cave features a broad, tabular main passage

with elliptical cross-sections, created by uniform dissolution. In this process, water dissolves rock consistently under saturated conditions, producing the rounded passage shapes characteristic of phreatic caves (Sweeting, 1973; Jennings, 1985; White, 1988; Ford and Williams, 2007, Fig. 6). The cave likely originated from rapid, focused groundwater flow along fractures and bedding planes within the volcanic substrate, which acted as natural drainage pathways. The cave transitions to a vertical channel-like conduit inset within the elliptical cross-section in its lower external section. Such features typically indicate the vadose zone in caves. The vadose zone refers to the unsaturated portion of the subsurface located above the water table, where water primarily flows downward under gravitational influence. The transition from phreatic to vadose conditions signifies a lowering of the water table (White, 1988; Ford and Williams, 2007).

At the cave, for the moment, seven sedimentological units have been identified: (i) Unit 7: Massive, poorly sorted coarse sands and gravels with a silty-clay matrix. (ii) Unit 6: A channel-form structure composed of coarse sands that incise into the underlying unit. (iii) Units 5–1: Predominantly debris facies deposits (Fig. 1b).

+21–24 m Terrace: The highest identified level consists of a strath surface with a superficial alluvial cover of very rounded, polymictic pebbles and clasts (Fig. 7a). No numeric dating is currently available for this layer.

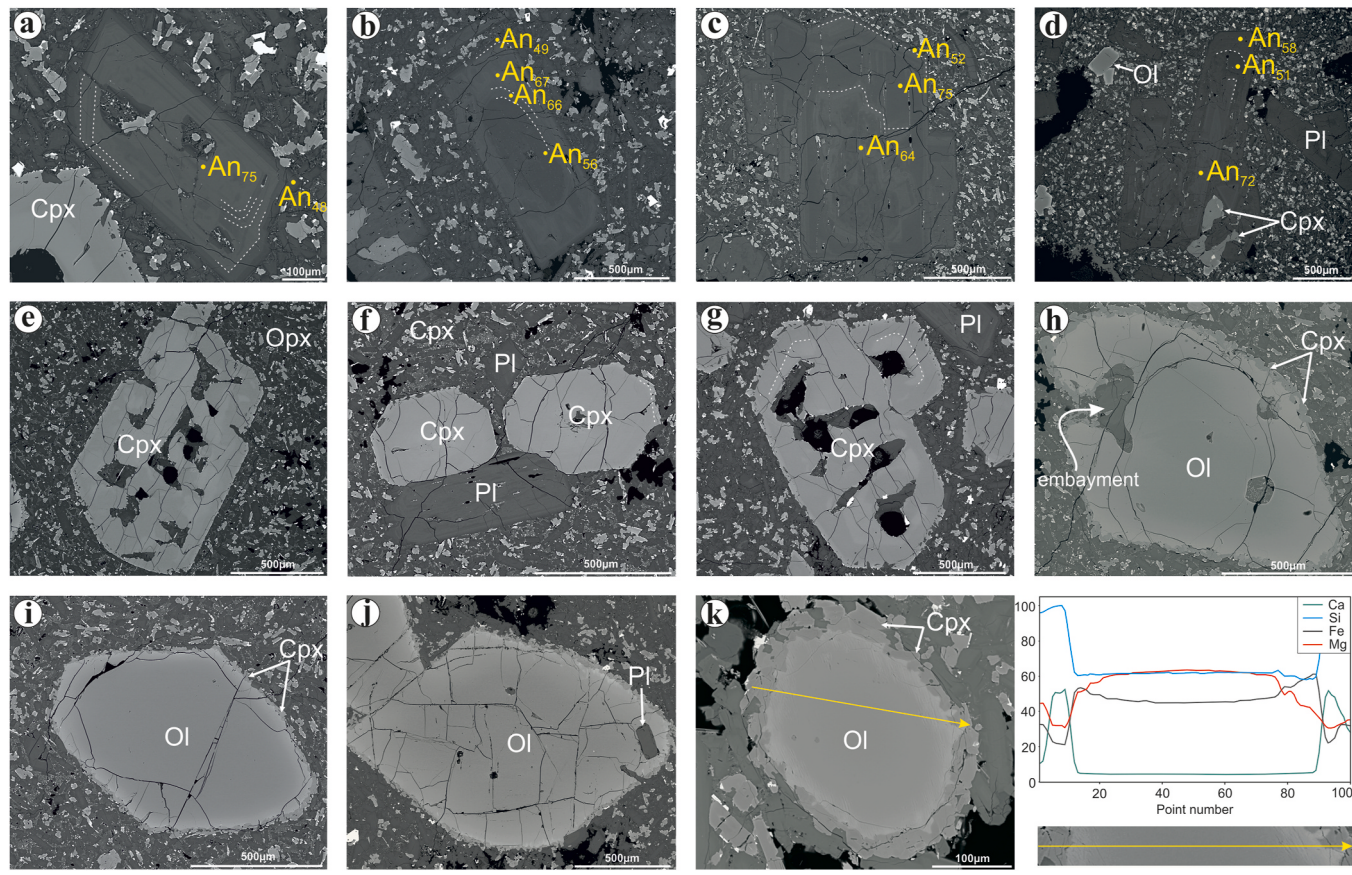


Fig. 11. BSE images of the main mineral phases from the crystal-rich lavas exposed on both the left and right banks of the Mastaraheghehat River: a) Normal oscillatory-zoned plagioclase phenocrysts with coarse-sieve texture (DVOL 10); b-c) Reverse oscillatory-zoned plagioclase phenocrysts (DVOL 10 and DVOL 9, respectively); d) Normal-zoned plagioclase (DVOL 4); e) Resorbed clinopyroxene (DVOL 9); f) Euhedral to subhedral crystals of clinopyroxene along with normal zoned plagioclase crystal (DVOL 9); g) Resorbed and slightly zoned phenocryst of clinopyroxene (DVOL 10); h) Embayed olivine with melt inclusions and rimed by clinopyroxene (DVOL 9); i) Phenocryst of olivine with Mg-rich core and Fe-rich rim (DVOL 9); j) Phenocryst of olivine with Mg-rich core and Fe-rich rim and inclusion of plagioclase (DVOL 10); k) Zoned olivine rimmed by clinopyroxene and the SEM-EDS analysis in line-scan mode showing main element variations along the line (DVOL 10). For abbreviations, refer to the figure captions of Figs. 8 and 10.

4.2. Lithostratigraphy and Petrology

The sample logs of the examined lava flows are presented in Fig. 2b, 5 and 6, 8a and 9a. As depicted in the field photographs of the outcrops (Fig. 2b, 6 and 8a and 9a), the primary lithologies exposed along the Mastaraheghehat River gorge are predominantly basaltic (trachy-) andesite and trachyandesite. Near Dalarik village and along both the left and right riverbanks, younger pyroclastic deposits, such as the Gyumri ignimbrite and its associated fallout unit from the Aragats stratovolcano, are also observable (Fig. 2). The lava flows analysed exhibit a variety of textures, observed in hand specimens, ranging from predominantly aphanitic (DVOL 1–3, 5–8, 13–14) to porphyritic/glomerophytic (DVOL 4, 9–12), with varying levels of porosity. On the right bank of the Mastaraheghehat River gorge, the lava flows are predominantly porphyritic or glomerophytic basaltic trachyandesite (Fig. 8). These are overlaid by aphanitic, and variably vesicular trachyandesite lava flows (Fig. 8).

On the left bank, the sequence is reversed, with the trachyandesite lava flow overlaid by porphyritic/glomerophytic basaltic andesite (Fig. 9). As shown in Fig. 9f-i, the trachyandesite lava flow exhibits a gradual transition from a vesicle-depleted lower section (e.g., DVOL 5) to an upper section (DVOL 6) with abundant small vesicles, which further transitions into a vesicular zone with varying vesicle concentrations and sizes (DVOL 7 and 8). A similar increase in vesicle concentration, from the basal (DVOL 9) to the upper (DVOL 12) part, is observed in the basaltic andesite (Fig. 9b–e). In the upper sections of

both lava flows, vesicles are partially filled with secondary minerals, such as calcite, exhibiting an amygdaloidal texture (Fig. 8b and 9b–c, f).

A comprehensive petrographic and qualitative analysis was conducted on 16 polished thin sections derived from the lava flows, with a focus on phenocryst abundance, mineralogical composition, and microtextural characteristics. The petrographic data categorise the volcanic rocks into two primary groups: crystal-poor aphanitic (DVOL 1–3, 5–8, and 13–14) and crystal-rich porphyritic/glomerophytic (DVOL 4, 9–12) variants (Figs. 8 and 9).

Crystal-poor aphanitic lavas: These lavas are characterised by a low abundance of phenocryst phases (<3 %), which include plagioclase, clinopyroxene, and orthopyroxene (Fig. 8b–g, 9f-i and 10), and feature groundmass textures that range from microcrystalline to intergranular and trachytic. In some instances, glomerophytic aggregates up to 1.5 mm in size are observed (e.g., Fig. 10a and d). The primary mineral phases identified in these samples include plagioclase, clinopyroxene, orthopyroxene, Fe-Ti oxides, and very rare alkali feldspar, with apatite as an accessory mineral (Figs. 8 and 10).

Plagioclase is the most abundant mineral phase in these lavas, occurring as phenocrysts, glomerocrysts, and in the groundmass (Fig. 10a–e). The crystals are primarily subhedral to euhedral and typically exhibit compositional zoning, ranging from An₃₈ to An₅₇ (Fig. 10a–e), classifying them as andesine to labradorite. Some phenocrysts show reverse zoning with Ca-rich rims (Fig. 10b and c and e). Certain plagioclase crystals also display fine resorption along the outer rims, characterized by a fine-sieve texture (e.g., DVOL 1), and commonly

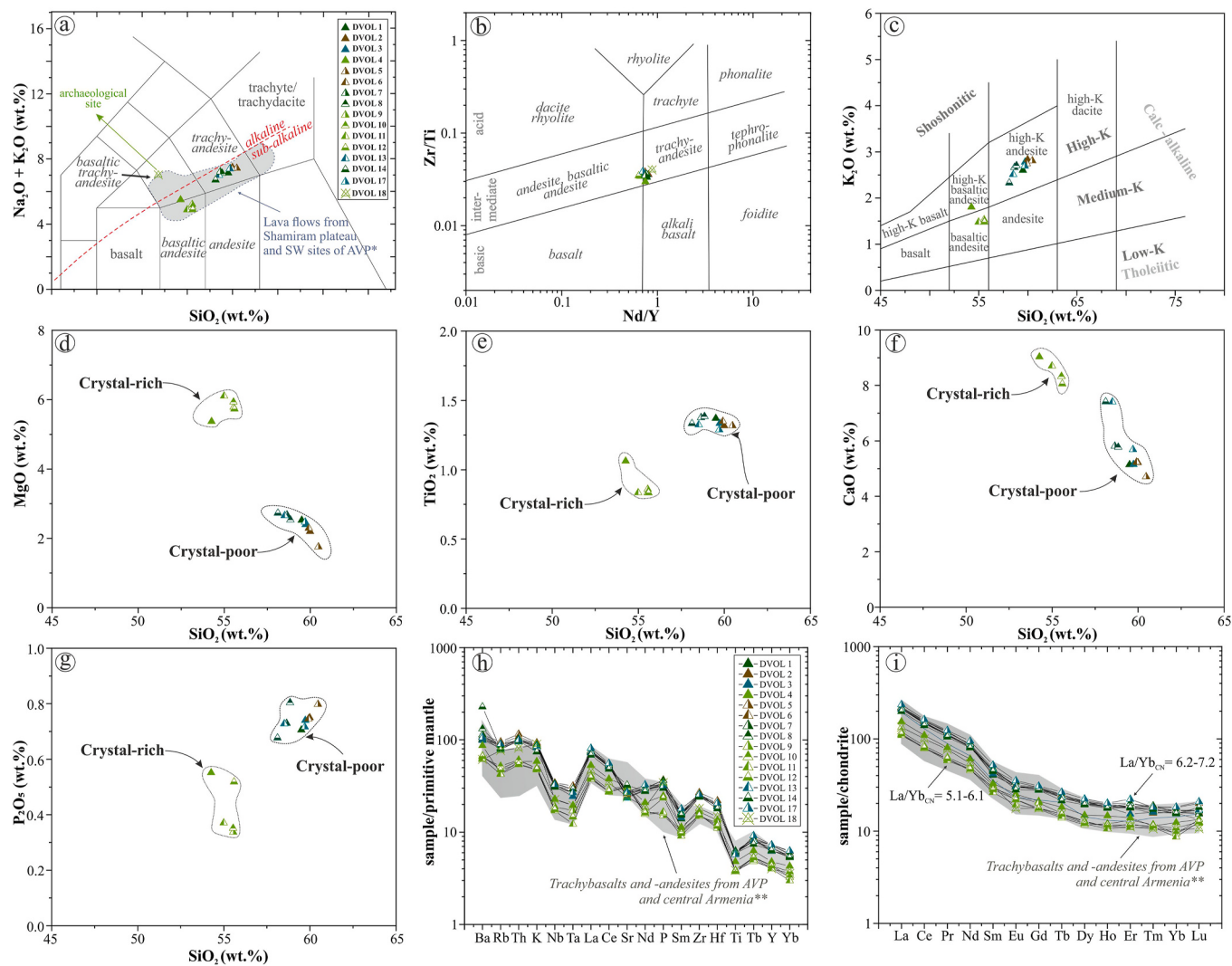


Fig. 12. a) Total alkali vs. SiO_2 classification diagram for studied samples from the Mastarahegheghat River Gorge (modified from Le Bas et al., 1986), alkaline/sub-alkaline boundary from Irvine and Baragar (1971). b) Zr/Ti vs. Nb/Y immobile element TAS proxy diagram (modified after Pearce, 1996). c) The K_2O vs. SiO_2 diagram after Peccerillo and Taylor (1976) indicates the studied rocks' medium-K to high-K calc-alkaline affinity. d-g) Major element variation diagrams (Harker diagrams). Element variation diagram of studied samples normalized to chondrite (i) and primitive mantle (h). Chondrite normalisation values from McDonough and Sun (1995) and Primitive Mantle values from Sun and McDonough (1989). *Data for lava flows from the Shamiram Plateau and southwestern (SW) sites of the AVP are sourced from Ghukasyan (1985) and Meliksetian (2012); **data for trachybasalts and trachyandesites from the AVP and central Armenia are taken from Meliksetian (2012) and Neill et al. (2015).

show simple polysynthetic twinning (Fig. 8e and 9i). In contrast, in DVOL 2 and DVOL 3, plagioclase shows fine resorption in both the outer rim and core, while a coarse-sieve texture is observed in a few crystals from DVOL 14. Inclusions of Fe-Ti oxides, apatite, and pyroxene are frequently observed (Fig. 10a-d, i-j).

The pyroxene minerals in these lavas show variation in both abundance and type. In most samples (e.g., DVOL 1, DVOL 7, DVOL 13, and DVOL 14), orthopyroxene is the dominant pyroxene, typically subhedral and occurs as individual phenocrysts up to 0.95 mm in length, within glomerophytic aggregates, and in the groundmass (Fig. 10g-i-j, l). Qualitative analyses indicate that these crystals are enriched in MgO, classifying them as enstatite and Mg-hypersthene. In contrast, orthopyroxene is rare in DVOL 2, DVOL 3, DVOL 5, and DVOL 6, where it primarily occurs in glomerophytic aggregates and the groundmass.

Clinopyroxene is the dominant pyroxene in certain samples (DVOL 2 and 3; Fig. 10h-k), occurring as subhedral to euhedral crystals up to 0.8 mm in length, with extinction angles ranging from 35° to 51°. These are classified as augite and diopside. Some clinopyroxene crystals exhibit slight chemical zonation, with Ca-rich cores (Fig. 10). Oscillatory-zoned

clinopyroxene with diopside cores is rare, primarily observed in DVOL 3, where the crystals are approximately 50 µm in length (Fig. 10k). Additionally, a few magnesium-rich pigeonite crystals are found in the groundmass (e.g., DVOL 1 and DVOL 14).

Opaque minerals reach up to 300 µm in size (e.g., DVOL 7; Fig. 10i) and are primarily composed of magnetite and titanomagnetite. Some of these minerals display a sandwich microstructure (e.g., DVOL 1; Fig. 10a) or a zonal ilmenite rim. The Fe-Ti oxides are randomly distributed throughout the groundmass, filling interstitial spaces and appearing as inclusions in pyroxene and plagioclase (Fig. 10), or forming part of glomerocrystic aggregates (e.g., Fig. 10a and i). The accessory mineral assemblage is dominated by elongated, needle-shaped fluorapatite microcrystals, typically found as inclusions within pyroxene and plagioclase (Fig. 10a-g-h, k-l) and as well as in the groundmass.

Crystal-rich porphyritic/glomerophytic lavas: These lavas are marked by a high crystal content, mainly feldspar, olivine, and pyroxene, with phenocrysts reaching up to 3.5 mm in length (Fig. 9c). The groundmass typically exhibits trachytic to intergranular textures, with the spaces between lath-shaped and prismatic plagioclase crystals filled

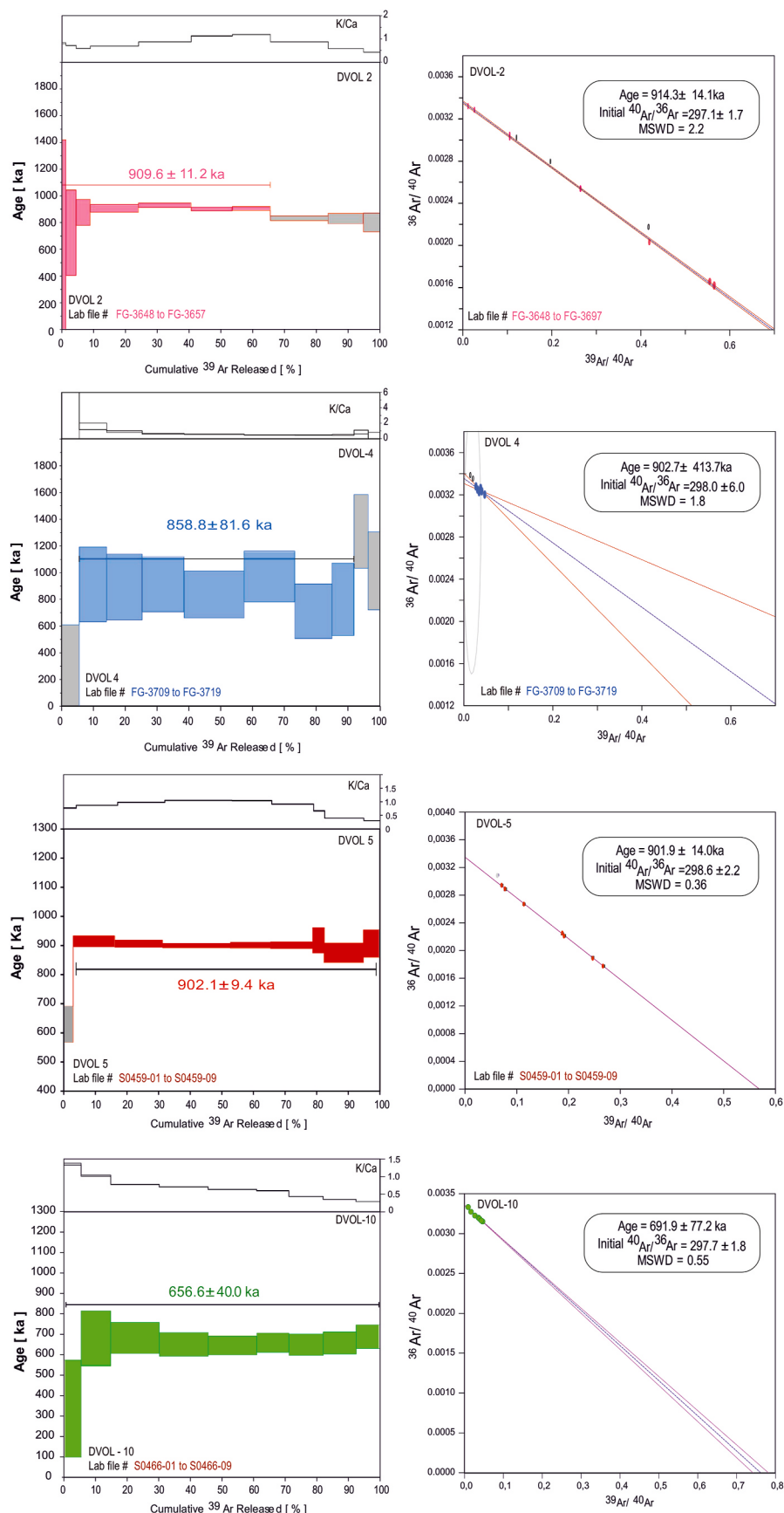


Fig. 13. $^{40}\text{Ar}/^{39}\text{Ar}$ Age spectra and Inverse isochron diagrams depicting $^{40}\text{Ar}/^{39}\text{Ar}$ experimental results from groundmass splits from samples DVOL 2, DVOL 4, DVOL 5, and DVOL 10. Grey-filled boxes are not included in the plateau age calculations. Grey ellipses correspond to data not included in the inverse isochron calculations. Uncertainties are ± 2 σ .

Table 1

Samples, depths, radionuclide concentrations, dose rates, De values and the final luminescence ages were obtained from the 4–11 polymineral fractions. Values are presented to two decimal places, and all calculations were made prior to rounding. Based on the results of the fading correction have been made and therefore the PIRIR225 age reflects the uncorrected age. * = overdispersion.

Sample ID	Depth (m)	Radionuclide activity (Bq kg ⁻¹)			External dose rate (Gy ka ⁻¹)			Cosmic dose rate (Gy ka ⁻¹)	Total dose rate (Gy ka ⁻¹)	n/N	OD* (%)	De (Gy)	Age (ka)
		U ²³⁸	Th ²³²	K ⁴⁰	Alpha dose rate	Beta dose rate	Gamma dose rate						
T4 upper unit	0.6	28.47	54.59	736.21	1.40 ± 0.29	2.47 ± 0.16	1.39 ± 0.09	0.25 ± 0.06	5.50 ± 0.35	20/20	13.6	51.2 ± 1.6	9.30 ± 0.66
T4 lower unit	1	34.1	53.66	573.7	1.49 ± 0.3	2.12 ± 0.13	1.3 ± 0.07	0.23 ± 0.06	5.15 ± 0.34	15/20	7.8	76.4 ± 1.7	14.84 ± 1.03
T3	0.7	18.82	39.34	355.25	0.98 ± 0.2	1.33 ± 0.09	0.86 ± 0.05	0.24 ± 0.06	3.41 ± 0.23	28/30	5.4	110.8 ± 1.9	32.53 ± 2.28

by pyroxene, olivine, and opaque minerals. Occasionally, glomerophytic aggregates, measuring ≥ 4.0 mm and consisting of plagioclase, clinopyroxene, olivine, and Fe-Ti oxides, are commonly observed (Fig. 8i and 9b-e).

Plagioclase is the most abundant mineral phase in these lavas, occurring as phenocrysts, glomerocrysts (up to 2.5 mm), and in the groundmass (Fig. 8i and 9b-e). The plagioclase crystals are primarily euhedral to subhedral, with some exhibiting a coarse-sieve texture in their cores. Polysynthetic twinning is commonly observed. A detailed study using optical and scanning electron microscopy of the crystal-rich lavas reveals significant variation in texture and zonation patterns (Fig. 11a-d). The plagioclase exhibits mainly normal (Fig. 11a and d) or (reverse)-oscillatory (e.g., Fig. 11b and c) zoning, with compositions ranging from An₄₈ to An₇₅, predominantly in the andesine to bytownite range. The groundmass also contains microcrysts of more felsic plagioclase, which are classified as labradorite in composition. Apatite inclusions are rare.

The primary pyroxene in these lavas is clinopyroxene, occurring as euhedral to subhedral crystals ranging from 0.4 mm to ≥ 2.3 mm in length, with inclined extinction angles ranging from 35° to 48°. Based on EDS analysis and petrographic observations, these crystals are classified as augite and diopside (e.g., DVOL 4 and DVOL 9), with some showing slight chemical zoning, particularly Ca-rich/diopsitic cores (Fig. 11g). In DVOL 10, a few subcalcic augite crystals are found as inclusions within plagioclase. Poikilitic augites containing rounded olivine inclusions and moderate to coarse resorbed crystals are also common in this sample (Fig. 11e and g). Additionally, single crystals of hypersthene and magnesian pigeonite are present (e.g., DVOL 9 and DVOL 10).

Olivine is the most abundant ferrromagnesian silicate, occurring in various forms, ranging from euhedral to resorbed subhedral crystals, with sizes from 0.25 mm to ≥ 1.5 mm in length. These crystals are found as single grains, clusters of two or three crystals, or as glomerocrysts. Most olivine phenocrysts exhibit zoning, with Mg-rich cores and Fe-enriched rims, often rimed by clinopyroxene (Fig. 11h-k). Some olivine crystals contain inclusions of plagioclase (Fig. 11j) or display embayment (Fig. 11h), while a few show signs of light iddingsitization (e.g., DVOL 9 and 10; Fig. 9d and e).

Opaque minerals, mainly magnetite and Ti-magnetite, occur as small, typically less than 100 μm , euhedral crystals. A few spinel-series crystals were also observed (e.g., DVOL 9). These minerals are randomly distributed throughout the rock, filling interstitial spaces in the groundmass and appearing as inclusions within clinopyroxene. Some of these minerals display a sandwich microstructure (e.g., DVOL 10). The accessory minerals consist mainly of elongated, needle-like apatite microcrystals, up to 200 μm in length, identified as fluorapatite through EDS analysis. These apatite crystals are common in the groundmass (e.g., DVOL 10; Fig. 11).

4.3. Whole-rock geochemistry: major and trace elements

The geochemical compositions of the volcanic samples analysed show significant variation, ranging from basaltic (trachy-) andesite (~ 52 – 56 wt% SiO₂) to trachyandesite (~ 58 – 60 wt% SiO₂), as shown in Fig. 12a.¹ This range of compositions is further demonstrated through the incompatible element Zr/Ti vs. Nb/Y ratio diagram (Fig. 12b). The samples plot below the transition line that distinguishes alkaline from sub-alkaline series (Fig. 12a), and according to the classification scheme of Peccerillo and Taylor (1976), they exhibit a medium-K to high-K calc-alkaline character (Fig. 12c). The basaltic (trachy-) andesites display higher MgO (5.38–6.11 wt%), CaO (8.06–9.03 wt%), and Na₂O/K₂O ratios (2.06–2.42) and noticeably lower TiO₂ and P₂O₅ concentrations compared to the trachyandesite samples (Fig. 12d–g; Table 2). Differences are also evident in the abundances of transition metals (Sc, Ni, Cr) and larger ion lithophile elements (LILEs), such as Sr and Ba (Table 2). The extended Primitive Mantle-normalized plot shows that the studied rocks exhibit pronounced negative Nb, Ta and Ti anomalies and positive Hf, Zr, and La anomalies (Fig. 12h). The chondrite-normalized REE patterns show enrichment in light rare earth elements (LREE), with a La/Yb_{CN} ratio ranging from 5.1 to 7.2, along with a slight negative Eu anomaly (Fig. 12i).

4.4. ⁴⁰Ar/³⁹Ar geochronology

Results are reported in Table 3 and Supplementary Table 3. ArArCalc software (Koppers, 2002) was used to calculate plateau ages, isochron regressions, weighted mean ages and probability of fit estimates. We adopted the criteria defining isochrons and plateau that are defined in Schaen et al. (2021). Results for groundmass splits of samples DVOL 2, 4, 5, and 10 are presented as age spectra and inverse isochrones in Fig. 13. Errors on ages are reported at 2σ and include all sources of error.

Sample DVOL 2. The step-heating experiment (Fig. 13) conducted on this sample allows the calculation of a plateau age with 65.3 % of total gas released (Table 3, Supplementary Table 3). Indeed, the last three steps gave younger ages that were not retained in the age calculation. Based on its LOI value (i.e., 1.17 %), this sample is unaltered. Nevertheless, given that this value is proximate to the threshold value (i.e., 1.0 % for basalt, as established by Faure and Mensing, 1993), a more sensitive index (Alteration Index, A.I., Baksi, 2007) was employed to evaluate the robustness of the plateau age. It is observed that the three steps that revealed the highest percentages of ⁴⁰Ar* have A.I. values that

¹ The studied samples exhibit a range of LOI values from 0.85 to 14.10 wt%, indicative of variable degrees of weathering by some of them. To facilitate accurate geochemical comparisons, major element concentrations have been normalized to an anhydrous basis, as presented in Table 2 and illustrated in the corresponding diagrams in Fig. 12.

Table 2

Whole-rock major and trace element compositions of Quaternary lava flows from both the left and right banks of the Mastarahegheghehat River Gorge (Armenia). LOI = loss-on-ignition, b.d. = below detection. The sample DVOL 18 is a polymictic weathered material from an archaeological site with high LOI.

Sample Number	DVOL 1	DVOL 2	DVOL 3	DVOL 4	DVOL 5	DVOL 6	DVOL 7	DVOL 8	DVOL 9	DVOL 10	DVOL 11	DVOL 12	DVOL 13	DVOL 14	DVOL 17	DVOL 18
Major oxides in wt.%																
Measured composition																
SiO ₂	58.20	59.20	57.30	53.10	60.60	59.50	57.10	57.80	55.70	55.30	53.40	54.70	57.90	55.80	57.50	40.20
Al ₂ O ₃	15.35	15.45	15.10	15.85	15.60	15.45	14.95	15.25	17.20	16.50	16.25	16.55	14.75	14.35	14.65	11.25
Fe ₂ O ₃	7.50	7.06	6.94	7.57	7.70	7.19	7.69	7.57	7.05	7.11	6.91	7.18	7.13	7.37	6.99	5.28
CaO	5.03	5.15	4.94	8.84	4.72	5.20	5.66	5.67	8.15	8.29	8.45	7.93	7.33	7.12	5.48	12.00
MgO	2.47	2.17	2.30	5.26	1.76	2.28	2.61	2.49	5.66	5.91	5.93	5.64	2.63	2.62	2.38	1.64
Na ₂ O	4.44	4.59	4.45	3.62	4.63	4.64	4.43	4.34	3.60	3.55	3.31	3.36	4.44	4.21	4.53	2.73
K ₂ O	2.54	2.79	2.66	1.76	2.81	2.72	2.59	2.65	1.49	1.47	1.43	1.45	2.48	2.23	2.59	2.71
Cr ₂ O ₃	b.d.	b.d.	b.d.	0.02	b.d.	b.d.	b.d.	b.d.	0.02	0.02	0.02	0.02	b.d.	0.00	b.d.	0.00
TiO ₂	1.34	1.30	1.28	1.04	1.32	1.34	1.34	1.36	0.84	0.83	0.81	0.82	1.31	1.28	1.24	0.84
MnO	0.11	0.10	0.11	0.12	0.14	0.12	0.13	0.14	0.12	0.12	0.12	0.12	0.13	0.13	0.13	0.07
P ₂ O ₅	0.69	0.74	0.71	0.54	0.80	0.74	0.71	0.79	0.33	0.35	0.36	0.51	0.72	0.65	0.69	0.75
SrO	0.05	0.06	0.05	0.07	0.05	0.05	0.06	0.05	0.06	0.06	0.06	0.06	0.05	0.07	0.05	0.06
BaO	0.08	0.08	0.08	0.07	0.09	0.08	0.09	0.10	0.05	0.05	0.05	0.05	0.08	0.17	0.08	0.05
LOI	1.05	1.17	1.14	2.19	1.27	1.03	1.68	2.01	0.14	0.85	1.25	1.32	2.56	3.78	3.80	14.10
Total	98.85	99.86	97.06	100.05	101.49	100.34	99.04	100.22	100.41	100.41	98.35	99.71	101.51	99.78	100.11	91.68
Normalized to an anhydrous basis																
SiO ₂	59.51	59.99	59.74	54.26	60.47	59.91	58.65	58.85	55.55	55.54	54.99	55.59	58.51	58.12	59.70	51.82
Al ₂ O ₃	15.70	15.66	15.74	16.20	15.57	15.56	15.36	15.53	17.59	16.57	16.73	16.82	14.91	14.95	15.21	14.50
Fe ₂ O ₃	7.67	7.15	7.24	7.74	7.68	7.24	7.90	7.71	7.21	7.14	7.12	7.30	7.21	7.68	7.26	6.81
CaO	5.14	5.22	5.15	9.03	4.71	5.24	5.81	5.77	8.33	8.33	8.70	8.06	7.41	7.42	5.69	15.47
MgO	2.53	2.20	2.40	5.38	1.76	2.30	2.68	2.54	5.79	5.94	6.11	5.73	2.66	2.73	2.47	2.11
Na ₂ O	4.54	4.65	4.64	3.70	4.62	4.67	4.55	4.42	3.68	3.57	3.41	3.41	4.49	4.39	4.70	3.52
K ₂ O	2.60	2.83	2.77	1.80	2.80	2.74	2.66	2.70	1.52	1.48	1.47	1.47	2.51	2.32	2.69	3.49
Cr ₂ O ₃	b.d.	b.d.	b.d.	0.02	b.d.	b.d.	b.d.	b.d.	0.02	0.02	0.02	0.02	b.d.	0.00	b.d.	0.00
TiO ₂	1.37	1.32	1.33	1.06	1.32	1.35	1.38	1.38	0.86	0.83	0.83	0.83	1.32	1.33	1.29	1.08
MnO	0.11	0.10	0.11	0.12	0.14	0.12	0.13	0.14	0.12	0.12	0.12	0.12	0.13	0.14	0.13	0.09
P ₂ O ₅	0.71	0.75	0.74	0.55	0.80	0.75	0.73	0.80	0.34	0.35	0.37	0.52	0.73	0.68	0.72	0.97
SrO	0.05	0.06	0.05	0.07	0.05	0.05	0.06	0.05	0.06	0.06	0.06	0.06	0.05	0.07	0.05	0.08
BaO	0.08	0.08	0.08	0.07	0.09	0.08	0.09	0.10	0.05	0.05	0.05	0.05	0.08	0.18	0.08	0.06
Total	100	100	100	100	100	100	100	100	100	100	100	100	100	100	100	100
Na ₂ O + K ₂ O	7.14	7.48	7.41	5.50	7.42	7.41	7.21	7.12	5.20	5.04	4.88	4.89	6.99	6.71	7.39	7.01
Na ₂ O/K ₂ O	1.75	1.65	1.67	2.06	1.65	1.71	1.71	1.64	2.42	2.41	2.31	2.32	1.79	1.89	1.75	1.01
Trace elements in ppm																
Sc						15.9	16.6	16.1	17.4	20.4	20.9	19.2	21	17.5	17	16.4
Ni						10	4	5	6	108	113	116	110	5	8	b.d.
Cr	12	7	5	146	10	7	8	9	166	182	178	173	6	13	8	29
V	154	160	129	153	157	159	152	172	128	128	122	123	170	168	157	130
Ba	704	709	692	608	792	755	796	924	469	448	438	463	747	1595	742	428
Ce	92.1	92.7	91.7	67	97	94.1	89.5	95.6	51.5	48.1	48.7	49.2	90.7	85.3	99.3	61.2
Cs	1.12	0.95	1.21	0.53	0.87	0.83	1.1	1.04	0.61	0.68	0.63	0.67	0.76	1.02	1.13	2.28
Dy	5.37	5.03	4.99	3.79	5.23	5.27	5.03	5.37	3.26	2.97	3.07	3.1	5.17	4.9	5.68	3.24
Er	3.02	2.94	2.53	2.31	3.31	3.07	3.03	3.33	1.97	2.17	1.82	1.93	3.02	2.97	3.67	1.84
Eu	1.77	1.78	1.73	1.46	1.82	1.77	1.98	1.76	1.36	1.27	1.12	1.28	1.79	1.63	2.05	1.02
Ga	19.4	19.9	19.3	17.5	18.4	18.8	18.4	17.7	16.7	17.1	16	16.7	18.5	17.3	18.3	13.5
Gd	5.74	6.01	5.94	4.34	6.18	6.05	6.12	6	4.17	3.55	3.63	3.63	5.71	5.73	6.34	3.66
Hf	6.1	6.28	5.96	4.17	6.79	6.11	5.97	5.8	3.41	3.72	3.91	3.59	5.84	5.53	6.36	4.53
Ho	1.02	1.07	1.02	0.83	1.03	1.09	1.04	1.12	0.63	0.68	0.6	0.66	1.1	1	1.14	0.63
La	50.6	50.4	50	36.4	52.2	51.3	50.1	52.1	28.1	26.4	25.8	26.8	49.7	47	55.8	31.8
Lu	0.42	0.4	0.34	0.34	0.43	0.51	0.39	0.42	0.31	0.34	0.32	0.43	0.46	0.53	0.27	
Nb	21.9	22.9	22.2	16.3	24.4	24.1	23.2	23.8	13.5	12.65	12.2	12.5	23	22.3	23.3	16.1
Nd	38.7	38.7	38.5	28.3	39.8	40.4	37.8	41	23	21.2	21.8	21.9	38.7	37.4	44.2	25.4

(continued on next page)

Table 2 (continued)

Sample Number	DVOL 1	DVOL 2	DVOL 3	DVOL 4	DVOL 5	DVOL 6	DVOL 7	DVOL 8	DVOL 9	DVOL 10	DVOL 11	DVOL 12	DVOL 13	DVOL 14	DVOL 15	DVOL 16	DVOL 17	DVOL 18
Pr	10.5	10.7	10.3	7.62	11.45	11.1	10.45	11.1	5.98	5.76	5.51	5.79	10.65	9.95	11.75	7.28		
Rb	55.6	56.6	52.3	27.3	60.6	58.2	51.8	52.2	30.7	33.1	26.9	30.1	50.1	50.1	57.2		48.6	
Sm	6.18	6.77	6.37	5.05	7.01	6.83	7.09	7.27	4.48	4.63	4.02	4.31	7.02	6.8	7.98		4.78	
Sn	1.5	1.3	1.2	0.9	2.4	2.5	1.5	1.3	0.9	1	1.1	1	1.4	1.8	1.9		1.2	
Sr	507	511	494	665	538	556	581	595	683	656	643	666	577	684	566		507	
Ta	1.1	1.1	1	0.8	1.3	1.2	1.1	1.2	0.7	0.6	0.5	0.6	1.1	1.2	1.1		0.8	
Tb	0.91	0.93	0.87	0.68	0.93	0.87	0.86	0.91	0.58	0.52	0.54	0.57	0.87	0.8	0.99		0.57	
Th	8.24	8.41	8.08	4.96	9.81	9.18	8.63	8.76	5.07	5.15	4.59	4.63	8.5	8.31	8.48		6.91	
Tm	0.42	0.4	0.41	0.29	0.47	0.47	0.48	0.45	0.28	0.3	0.28	0.29	0.44	0.44	0.46		0.27	
U	2.31	2.36	2.26	1.53	2.66	2.61	2.3	2.24	1.28	1.26	1.48	1.22	2.41	2.41	3.06		1.72	
W	1.3	1.5	1.6	1.3	1.2	2	1	1.1	1.1	0.6	<0.5	1.8	0.9	1	0.9		0.8	
Y	28.2	28.4	28.5	21.7	32.9	33.2	30.9	32.9	19.9	18.7	18.3	19.6	30.9	28.9	33.1		18.3	
Yb	2.84	2.74	2.67	2.11	2.85	3.05	2.71	2.83	1.61	1.6	1.47	1.84	2.65	2.62	3.1		1.76	
Zr	268	278	272	186	301	289	290	174	171	166	170	281	274	286	286		202	
La/Yb _{EN}	7.00	6.93	7.07	6.10	7.02	7.09	6.19	7.24	5.06	5.09	5.64	5.12	6.79	7.06	6.66		7.63	

are either slightly higher or equivalent to the cut-off value, which corresponds to the unaltered/altered limit. Therefore, it provides confidence that the plateau age is geologically significant. There is no evidence of $^{40}\text{Ar}^*$ excess or mass fractionation, as the $^{40}\text{Ar}/^{36}\text{Ar}$ intercept values calculated for the inverse isochron (Fig. 13, Table 3) are within uncertainties of the current atmospheric value. The age we retain for this sample is the plateau age (909.6 ± 11.2 ka), which is equivalent to the inverse isochron age.

Sample DVOL 4. The plateau age, as determined from the step-heating experiment, is 858.8 ± 81.6 ka (Fig. 13, Table 3), with 86.4 % of the total gas released. The inverse isochrone age is very imprecise (902.7 ± 413.7 ka) because of a poor spread of the experimental points along the isochrone. The $^{40}\text{Ar}/^{36}\text{Ar}$ intercept value is atmospheric (297.96 ± 6.00), evidence of no excess $^{40}\text{Ar}^*$. The relatively poor precision, given the age of the sample, is attributed to the low percentages of $^{40}\text{Ar}^*$ detected, at approximately 2–4 %. This may be indicative of a high degree of atmospheric contamination, which is not surprising because of the high vesicularity of the sample. The LOI value of this sample is indeed high for the $^{40}\text{Ar}/^{39}\text{Ar}$ standards (i.e., 2.29 %; Faure and Mensing, 1993), and all the calculated A.I. values are approximately 20 times the threshold value (Supplementary Table 3). As a consequence, the plateau age may be inaccurate and not geologically significant.

Sample DVOL 5. The step-heating experiment (Fig. 11) conducted on this sample allows the calculation of a plateau age with 97.4 % of total gas released (Table 3, Supplementary Table 3). There is no evidence of $^{40}\text{Ar}^*$ excess or mass fractionation, as the $^{40}\text{Ar}/^{36}\text{Ar}$ intercept values calculated for the inverse isochron are within uncertainties of the current atmospheric value (298.6 ± 2.2). The age we retain for this sample is the plateau age (902.1 ± 9.4 ka), which is equivalent to the inverse isochron age.

Sample DVOL 10. The step-heating experiment (Fig. 13) conducted on this sample allows the calculation of a plateau age with 100 % of total gas released (Table 3, Supplementary Table 3). There is no evidence of $^{40}\text{Ar}^*$ excess or mass fractionation, as the $^{40}\text{Ar}/^{36}\text{Ar}$ intercept values calculated for the inverse isochron are within uncertainties of the current atmospheric value (297.7 ± 1.8). The age we retain for this sample is the plateau age (656.6 ± 40.0 ka), which is equivalent to the inverse isochron age. However, it should be noticed that the inverse isochron with a 5 % spreading factor is not valid, and the isochron is therefore not very useful in this case.

5. Discussion

The petrographic and geochemical analyses, and geomorphological studies, combined with new $^{40}\text{Ar}/^{39}\text{Ar}$ age data from volcanic samples of the Mastarahegheghat River Gorge, reveal distinct characteristics that offer valuable insights into their origin and evolution.

5.1. Petrographic and petrological characteristics of crystal-poor and crystal-rich lavas

The petrographic data demonstrate a distinction between two groups of lavas: crystal-poor and crystal-rich variants. The crystal-poor lavas, such as DVOL 1, 2, 7, and 8, display relatively simple mineral compositions, with plagioclase and pyroxene phenocrysts in trachytic to intergranular groundmass. The moderate to high vesicularity observed in these samples, especially in DVOL 1, 7, and 8, suggests relatively rapid cooling rates and/or degassing processes (Thordarson et al., 1996). This may indicate that these flows likely resulted from the eruption of volatile-rich magma at a moderate to relatively high eruption rate (Thordarson and Self, 1993).

The plagioclase in these crystal-poor lavas ranges from andesine to labradorite in composition, with zoning patterns (such as reverse zonation; see Fig. 10b and c and e) that suggest changes in the crystallization conditions and indicate a mafic magma input (Gevorgyan et al.,

Table 3
Summary of $^{40}\text{Ar}/^{39}\text{Ar}$ data from incremental heating experiments on groundmass splits.

Sample	wt.	K/Ca	Total Fusion	Age Spectrum				Isochron Analysis			
				Increments		^{39}Ar	Age \pm	$^{40}\text{Ar}/^{36}\text{Ar}$		$2\sigma^{(1)}$	F
				(%)	(ka)	(%)	(ka)	MSWD	n/N	MSWD	Intercept
DVOL 2 FG-3648 to FG- 3657	142	0.78	872.4	\pm	17.3	607–959	65.5	909.6	\pm	11.2	1.51
DVOL 4 FG-3709 to FG- 3719	129	0.67	851.4	\pm	76.6	723–1089	86.4	858.8	\pm	81.6	0.70
DVOL 5 S0469-01 to S0469-02	6	0.51	892.9	\pm	13.6	0.65–2.8	97.0	902.1	\pm	9.4	0.20
DVOL 10 S0466-01 to S0466-02	6	0.43	644.2	\pm	52.8	0.65–2.8	100.0	656.6	\pm	40.0	0.30

Ages calculated relative Acs-2 at 1.1891 Ma (Niepolo et al., 2017) and the total ^{40}K decay constant of Renne et al. (2011) (1): Full external error. F: Spreading factor of Jourdan et al. (2009).

2018). The fine resorption textures observed in some plagioclase crystals (Figs. 9 and 10) likely result from late-stage changes in the magma composition, such as partial dissolution due to reaction with more mafic melt (Renjith, 2014). Similarly, the presence of orthopyroxene, particularly enstatite and Mg-hypersthene, in these samples points to crystallization from a more magnesium-rich melt, with compositions consistent with those found in basaltic andesites (Ghukasyan, 1985).

In contrast, the crystal-rich lavas (e.g., DVOL 4, 9, 10, 12) contain a higher proportion of feldspar, pyroxene, and olivine phenocrysts, suggesting a slower cooling rate. This can be linked to the presence of a deeper or more isolated magma chamber, where the magma experienced prolonged cooling and crystal growth. The higher phenocryst content also likely points to a more evolved magmatic process, with fractional crystallization and possibly magma mixing contributing to the development of these crystal-rich lavas. The presence of both pyroxene and olivine phenocrysts, in particular, may suggest that the system underwent multiple stages of cooling and differentiation. The moderate to high porosity in these lavas is consistent with the presence of abundant phenocrysts, which would create more interstitial spaces. These lavas exhibit more complex textures, such as trachytic to intergranular groundmass with pyroxene and olivine filling interstitial spaces between plagioclase crystals. The presence of glomerophyritic aggregates, as seen in DVOL 4 and 9, indicates magma mixing or multiple crystallization events (complex and repeated magma process; e.g., Ikeda et al., 2002; Crabtree and Lange, 2011; Renjith, 2014), further suggesting a more complex magmatic history. The olivine phenocrysts in the crystal-rich lavas typically show zoning, with Mg-rich cores and Fe-enriched rims, indicative of fractional crystallization processes in a cooling magma chamber (e.g., Liu et al., 2015). Additionally, the presence of melt inclusions and embayments in some olivine crystals suggests that magma mixing was a prevalent process in the system (Liu et al., 2015; Lynn et al., 2017).

The presence of Fe-Ti oxides (magnetite, Ti-magnetite, and ilmenite) in both crystal-poor and crystal-rich lavas indicates crystallization under relatively oxidizing conditions, consistent with the medium-to-high-K calc-alkaline nature of the magmas in AVP (Ghukasyan, 1985). Furthermore, the occurrence of poikilitic augites containing rounded olivine inclusions in DVOL 10 and the detection of hypersthene and magnesian pigeonite in some samples further suggest magma evolution through cooling and crystallization at various stages. The mineral assemblage, composition, and textural characteristics of the analysed lava flows suggest a correlation with those from the southwestern and southern slopes and plateaus of the AVP, as documented by Ghukasyan (1985), thereby allowing their attribution to the first and second eruptive stages of the AVP.

5.2. Geochemical insights

The shaded field outlines the compositional range of the studied lava flows, along with those previously reported from the Shamiram plateau and southwestern sites of the AVP (Ghukasyan, 1985; Meliksetian, 2012), demonstrating a strong geochemical correlation (Fig. 12a-h-i). The negative anomalies in Nb, Ta, and Ti, along with the positive anomalies in Hf, Zr, Ce, and La, observed in the primitive mantle-normalized variation diagram, are indicative of subduction-related magmatic processes (Pearce et al., 1990; Keskin, 2003; Meliksetian et al., 2014; Neill et al., 2015; Gevorgyan et al., 2018). These features are typical of magmas that have been influenced by fluids or melts derived from a subducting slab, which would deplete the magma in Nb and Ta while enriching it in large-ion lithophile elements (LILEs) such as Ce and La (e.g., Neill et al., 2015). This geochemical signature is consistent with the high-K calc-alkaline nature of the samples, suggesting that the magma source may have been affected by slab-derived fluids or melts (Briqueu et al., 1984; Keskin et al., 1998; Pearce et al., 1990).

The chondrite-normalized REE patterns further support the

subduction-related origin of the magmas. The observed enrichment in light rare earth elements (LREE) and the absence or slight negative Eu anomaly suggest that the magmas underwent a degree of fractional crystallization, which preferentially removed heavy rare earth elements (HREE) from the liquid. The (La/Yb)_{CN} ratio of 6.1–7.1 indicates a significant LREE enrichment (Fig. 12, Table 2), a common feature in subduction-zone magmas (Neill et al., 2015).

5.3. Geomorphological and geochronological evolution of the study area based on strath terrace sequence

5.3.1. Records of alluvial deposits from local fluvial sequences in the wider region

The geomorphological development of the study area reflects a dynamic interplay of fluvial, tectonic, volcanic, and climatic processes that have shaped the landscape from the Early Pleistocene to the present. This evolution can be reconstructed through the analysis of the strath terrace and volcanic rock sequences, both within the immediate Mastaraheghehat River Gorge and in the broader Armenian Highland region.

The broader region has been largely overlooked by researchers regarding the identification and evolution of fluvial sequences. Some outstanding works, such as that of Sayadyan (2006, 2009), assert that the western Ararat Depression is distinguished by a Quaternary sequence marking the Middle Pleistocene onset, as evidenced by lake-alluvial deposits comprising *Mammuthus trogontherii chosaricus* and *Palaeoloxodon antiquus*. These deposits also contain *Dreissena dilluvii Abich* mollusks within coarse fluvial sediments. The semi-arid climate of the time supported steppe landscapes with forested river valleys. Middle Pleistocene alluvial deposits, showing two-stage stratification, formed during two major glaciation phases on Aragats. In the Late Pleistocene, tectonic activity deepened river valleys, leading to the thickest sediment accumulation in the Khor-Virap area. Five distinct floodplain terraces are evident, with the first four correlating to glacial and postglacial phases, and the fifth primarily dating to the Middle Holocene. Karampaglidis et al. (2025) analysed alluvial records from the northeastern Ararat Depression, uncovering a complex interplay of tectonic, volcanic, and climatic factors that shaped its geomorphology from the late Early Pleistocene to the Holocene. Fluvial deposits from the late Early to Middle Pleistocene formed under tectonic uplift, reflecting basin infill during a period of intense volcanic activity. The Late Pleistocene sequence consists of five layers: the uppermost, formed during the MIS7–MIS6 transition, indicates glacial conditions and local volcanism. The next layer represents channel fills under cold, dry conditions at the end of the Middle Pleistocene. The third terrace, formed during the arid, cold conditions of MIS4, was influenced by both volcanic and climatic factors. The fourth layer, dated to 30 ka, marks fluvial infilling before the Last Glacial Maximum. In the Holocene, extensive fluvial fans, including the Vedi River fan, developed across the Ararat Depression, truncating Late Pleistocene deposits and hosting Late Neolithic sites.

Additional terrace system was studied in the upper and middle Kura Valley. In the upper Kura valley, a total of 17 fluvial terraces (T1 to T17), along with the modern floodplain, were identified using a semi-automated mapping method (TerEx Toolbox), complemented by manual digitization and field validation (Boichenko et al., 2025). Terrace elevations range from 10 to 22 m for T1 (the youngest) to approximately 690 m for T17 (the oldest), measured above the present-day river level. Cosmogenic nuclide burial dating using ¹⁰Be, ²⁶Al, and ²¹Ne was employed to constrain terrace chronologies. Four terrace levels were sampled: Gldani (GLD) – T8, Mukhatverdi (MKG) – T12, Kashueti (KSH) – T17, and Makhata (MKH) – T12. The estimated minimum burial ages are approximately ~670 ka for MKG (T12), 440 ka for KSH (T17), and ~380 ka for MKH (T12). These are interpreted as minimum ages due to potential post-burial nuclide production and the possibility of complex exposure histories. Based on regional stratigraphic context, the highest terrace (T17) lies above Agchagylian

sediments and exhibits angular unconformities. Therefore, the fluvial terraces must postdate the Agchagylian deposits (Late Pliocene–Early Pleistocene), implying that they are not older than approximately 1600–2400 ka (Boichenko et al., 2025).

Where in the Middle Kura valley, a five-layer fluvial sequence has been identified. The oldest terrace, T0 (47–36 ka), represents significant alluvial deposition. Terrace T1 (27–13 ka) indicates substantial sediment accumulation during the Last Glacial Maximum and Late Glacial periods. T2, dated to 11.2–3.6 ka, marks the Late Glacial-Holocene transition, reflecting increased hydrological activity. Terrace T3 (3.6–2.2 ka) is characterized by the development of hydromorphic soils. The youngest terraces, T4 and T5 (2.2–0.14 ka), reflect the influence of the Derbent regression and the Little Ice Age on sedimentation dynamics (Ollivier et al., 2015; von Suchodoletz et al., 2016). At Lake Van, Turkey, a fluvial sequence of four Upper Pleistocene terraces has been identified (Schweizer, 1975; Kuzucuoğlu et al., 2010). Terrace T1 (+108–98 m), composed of shoreface sands and gravels, predates 105 ka. T2 (+79–77 m), formed by fan deltas overlying sandy bottomsets, dates to after 105 ka. T3 (+49–46 m) consists of shallow-depth sediments and fan deltas, with ages ranging from 26 to 20 ka. T4 (+23–20 m) is composed of exhumed alluvial and shallow-water lake sediments, dating to post-20 ka. These terraces reflect lake-level variations and their driving mechanisms.

5.3.2. Landscape and geochronological reconstruction of the study area through the fluvial sequence of the Mastaraheghehat River

Strath terraces, which reflect episodic fluvial incision, sediment deposition, are critical for reconstructing past environments due to their widespread distribution and well-preserved records across various latitudes. Their sedimentological characteristics, stratigraphic structures, and the presence of artifacts, fossils, and pollen offer valuable insights into the environmental conditions of their formation and their connections to major climatic and tectonic events. As key geomorphic markers, strath terraces help identify glacial-interglacial cycles and tectonic activity, shedding light on base-level changes, incision rates, and the relationship between climatic and crustal fluctuations that shape landscape evolution (Bull, 1977, 1991; Gibbard, 1988; Antoine, 1994, Antoine et al., 2000; Bridgland, 1994, 2000; Stokes and Mather, 2000; Van den Berg and Van Hoof, 2001; Gibbard and Lewin, 2002; Bridgland and Westaway, 2008; Cunha et al., 2008; Westaway et al., 2009; Kuzucuoğlu et al., 2010; Ollivier et al., 2010, 2015; Silva et al., 2017; Stokes et al., 2017; Karampaglidis et al., 2020; Benito-Calvo et al., 2022). The geomorphological evolution of the study area is interpreted through the sequence of five strath terrace levels and associated surfaces. Based on available numerical dating and geomorphological evidence at Mastaraheghehat River, five terraces provide a detailed record of the landscape evolution (Fig. 14).

The +21–24 m terrace represents the highest strath surface in the study area and overlying a basaltic andesite flow dated to 656.6 ± 40 ka, covered by a thin layer of very rounded, polymictic pebbles and clasts (Fig. 7a). It likely formed during an early phase of fluvial activity when the Mastaraheghehat River was at a significantly higher level. According to diverse studies in other rivers (Antoine, 1994; Mania, 1995; Antoine et al., 2004, 2007; Bridgland and Westaway, 2008; Vandenberghe, 2008; Benito-Calvo et al., 2022), this terrace indicates a period of prolonged stability in river incision, allowing for strath formation and minor sediment deposition. Although the lack of numerical dating precludes precise chronological placement, the terrace's considerable elevation suggests it predates the other identified surfaces. Its stratigraphic position above a lava flow dated to 656.6 ± 40 ka, combined with this revised geochronology, supports an estimated minimum age of ≥656 ka.

The +11 m terrace is located near the entrance of the Dalarik-1 Cave. The plain in front of the cave, part of the +11 m strath terrace formed by fluvial erosion during a period of river stability. The cave formed along the lithological boundary between basaltic trachyandesite flow (dated to

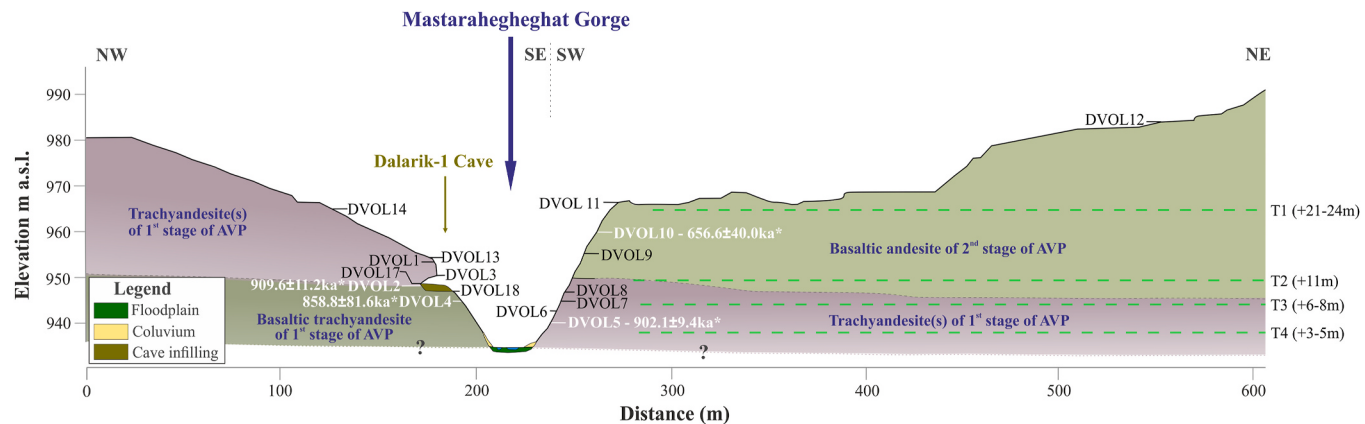


Fig. 14. Schematic cross-sectional profile of the Mastarahegheghat Gorge, illustrating the elevation (m a.s.l.) of lava flow sequences exposed along the gorge's sides, along with sample logs and terraces. *Ages derived from $^{40}\text{Ar}/^{39}\text{Ar}$ dating in this study

858.8 ± 81.6 ka) and trachyandesite unit (909.6 ± 11.2 ka; Figs. 13 and 14). The contact zone between these units is brecciated, likely resulting from thermal and mechanical fragmentation during emplacement or cooling of the upper flow. This brecciated interface created a zone of structural weakness that was particularly susceptible to erosion and water infiltration, ultimately facilitating the cave's development. The terrace formation indicates a stable fluvial regime where weathering and erosion are the dominant processes. Later, the cavity is mainly infilled by debris facies deposits. The artifacts and faunal remains embedded in the later contribution suggest that the human occupation occurred after the formation of the cave.

The +6–8 m terrace presents distinct characteristics depending on its location: In the gorge, Thin strath terrace (0.5–1 m thick) dated to 32.5 ± 2.3 ka (OSL), capped by debris talus (Fig. 7b–Table 1), corresponding to an incision rate of 0.18–0.25 mm/yr. At the eastern gorge opening: A strath surface with a thin cover of polymictic, rounded, very coarse clasts. Reflects a period of incision and subsequent stabilization, with differences in sediment cover due to localized geomorphic processes. Coarse fluvial sediments are interpreted as associated with glacial periods (Gibbard, 1988; Allen and Gibbard, 1994; Gibbard and Allen, 1994; Antoine et al., 2000, 2007; Bridgland, 2000; Vandenberghe, 2008; Wolf et al., 2022), which indicate periods of increased aggradation in the floodplain (Wolf and Faust, 2015). The dating places this terrace within the Late Pleistocene, represents fluvial valley infilling with coarse sediments before the onset of the Last Glacial Maximum, indicating a fluvial response to climatic shifts, potentially linked to the MIS 3–2 transition.

The +3–5 m terrace is a thin sediment layer (1–3 m) overlying bedrock, consisting of two units: Lower Unit: Poorly sorted clast-supported deposits with large, sub-rounded clasts in a silty-clay matrix, indicating high-energy flow events dated by OSL 14.8 ± 1 ka, which correspond to an incision rate of 0.34 mm/yr (Table 1). And an Upper Unit: Moderately sorted clast-supported deposits with smaller, rounded pebbles and clasts dated by OSL 9.3 ± 0.6 ka (incision rate of 0.32 mm/yr), and capped by debris talus (Table 1). This represents a transition from high-energy depositional conditions to lower-energy events and subsequent mass wasting. The formation of the terrace spans the Late Glacial and early Holocene, reflecting climatic fluctuations and the transition from glacial to interglacial conditions. An early Holocene occupation was found within this terrace, fitting in age with the current independent chronology of the terrace (Arimura et al., 2018). The lower unit could be related to Older Dryas climatic event during the deglaciation period at the end of the Pleistocene (~14,000 years ago), and represent a temporary return to colder conditions amid the transition from the Last Glacial Maximum (LGM) to the relatively warm Bølling-Allerød interstadial (~14,700–12,900 years ago, Björck et al., 1996; Rasmussen et al., 2006; Stuiver et al., 1995; Carlson, 2010;

Schwander and Stauffer, 1984). The upper unit could be related to the Early Holocene Cold Event, often referred to as the 8.2 ka event, which is one of the most significant climatic anomalies during the Holocene epoch. It represents a brief but pronounced cooling episode that lasted between 150 and 400 years, interrupting the otherwise warm and stable climate of the Early Holocene (Kobashi et al., 2007; Alley and Ágústsdóttir, 2005; Severinghaus and Brook, 1999).

The floodplain (youngest) consists of sediments deposited during overbank flooding events. These deposits are approximately 1 m thick and consist of sands, silts, and clays, enriched with organic matter and bioturbation, and reflect a recent fluvial activity and sedimentation under current hydrological conditions. The floodplain unit represents the youngest stage of geomorphic evolution, indicating an active fluvial system with periodic flooding and sediment transport.

Collectively, the terrace sequence of the Mastarahegheghat River records significant geomorphological transformations driven by glaciation, climatic fluctuations, tectonic activity, and phases of human occupation. When compared to terrace systems across the Armenian Highland and adjacent regions, this sequence provides critical insights into Quaternary landscape evolution and the broader climatic–tectonic framework that has shaped the region's geomorphology.

6. Conclusive remarks

The paper presented the lithostratigraphy, geochronology, and geomorphology, providing the context for the early occupation at the Dalarik-1 Cave Lower Paleolithic site. The depositional history of the Mastarahegheghat River Gorge includes.

I. Petrological and geochemical evidence indicate that volcanic rocks from the Mastaraheghehat River Gorge originated from a subduction-related magmatic system, with fractional crystallization and magma mixing being the key processes responsible for the compositional diversity observed during its evolution. The crystal-rich and crystal-poor lava groups reflect different stages of magma evolution, with crystal-rich lavas undergoing greater crystallization and differentiation. Furthermore, the presence of variable zonation patterns—such as reverse or reverse-oscillatory zoning—in phenocrysts and glomerophytic aggregates offers further evidence for magma mixing or recharge. Geochemical features, such as negative Nb and Ta anomalies and LREE enrichment, support a subduction-modified mantle source, possibly influenced by slab-derived fluids or melts.

II. The $^{40}\text{Ar}/^{39}\text{Ar}$ geochronological data for the studied trachyan-desites (DVOL 2 and DVOL 5) show reliable plateau ages of 909.6 ± 11.2 ka and 902.1 ± 9.4 ka, respectively, supported by low alteration indices and no evidence of $^{40}\text{Ar}^*$ excess. Based on age

lithostratigraphy, and geochemical and mineralogical patterns, these samples are linked to the first AVP eruption stage (Gevorgyan et al., 2018, 2020). In contrast, the plateau age of sample DVOL 4 (858.8 ± 81.6 ka) is less precise, with high atmospheric contamination, suggesting it may not be geologically significant but still records the first stage of volcanic activity in the AVP, similar to basaltic (trachy-)andesites in the S and SW.

- III. The exposed volcanic history at the Mastaraheghehat River Gorge, as recorded by lava flows, reveals two phases of the first stage (DVOL 4, DVOL 2) and one phase of the second stage (DVOL 9 to 12) of the AVP eruptions. It is less likely that Paleolithic hunter-gatherers' activities will be preserved within such conditions. Those eruptive landscapes are erosive in their depositional characteristics.
- IV. The earliest evidence for the river incision forming the +21–24 m strath terrace during a stable phase. The +11 m terrace formed during river stability. Those river erosions created the Dalarik-1 Cave in which the Lower Paleolithic artifacts and faunal remains were embedded after the cave's formation. The +6–8 m terraces as it adjusted to climatic or tectonic changes, including periods of increased discharge or base level drop. This terrace is dated to 32 to 32.5 ± 2.3 ka (OSL). After that, the Late Glacial Transition (+3–5 m Terrace – Older Dryas) is dated to 14.8 ± 1 ka. The subsequent stabilization and Holocene climatic amelioration allowed for the deposition of the upper unit. This phase is dated to 9.3 ± 0.6 ka. Finally, modern floodplain formation from current river dynamics reflects recent hydrological and geomorphic processes.
- V. The Dalarik-1 Cave, which hosts a Lower Paleolithic site, likely formed after the incision of the local gorge following the deposition of the youngest volcanic unit of the plateau ($\sim 656.6 \pm 40.0$ ka). This incision led to the development of four fluvial terraces (T1–T4), with the lower terraces (T3 and T4) dated between ~ 35 and 9 ka, reflecting periods of climatic and/or tectonic activity. The cave likely formed during a stable river phase associated with the formation of the T2 terrace, through combined chemical and mechanical erosion of the volcanic bedrock (first AVP eruption stage). Its formation is therefore constrained to between ~ 656.6 ka and 32.5 ± 2.3 ka (T3). Archaeological material recovered from the cave, including Lower Paleolithic artifacts, indicates human occupation occurred after its formation, offering valuable insights into early hominin activity in the region. Future research on the interplay and chronology of those two depositional mechanisms of the cave deposits and terrace will provide a more refined basis for the study of the site formation processes of the Lower Paleolithic occupation of Dalarik-1 Cave.

The geomorphological evolution of the study area demonstrates a dynamic interplay between climatic variability, tectonic uplift, and fluvial processes. The strath terraces serve as markers of episodic incision and stabilization, preserving evidence of paleoenvironmental conditions and human occupation over tens of thousands of years. The combination of geomorphology, volcanology, and numerical dating provides a comprehensive framework for understanding the region's landscape evolution.

CRediT authorship contribution statement

HG: Writing – original draft, Review & editing, Investigation, Methodology, Formal analysis, Software, Visualisation, Conceptualization, Data curation. TK: Writing – original draft, Review & editing, investigation, Field studies, Methodology, Software, Visualisation, Conceptualization. AMB: Review & editing, investigation, Field studies, Funding acquisition, Conceptualization. SN and KF: Review & editing, Formal analysis, Investigation, Software. IO: Investigation, Field studies. AP & BG: Investigation, Field studies, Review & editing, Validation. All

authors contributed to the scientific discussions and comments to the manuscript and have approved the submitted version.

Declaration of competing interest

The authors declare that they have no known competing financial interests or personal relationships that could have appeared to influence the work reported in this paper.

Acknowledgments

The Authors would like to thank the director of the Institute of Archaeology and Ethnography of the National Academy of Sciences of the Republic of Armenia, Dr. Arsen Bobokhyan, for his support regarding the permits for fieldwork investigations and sample transportation. Fieldwork, laboratory analyses and syntheses were funded by The Gerda Henkel Stiftung grant (n. AZ 10_V_17 and n. AZ 23/F/19), the Fritz-Thyssen Foundation grant awarded for the project "Pleistocene Hunter-Gatherer Lifeways and Population Dynamics in the Ararat (paleo-lake) Depression, Armenia", and The European Research Council grant N 948015: "Investigating Pleistocene population dynamics in the Southern Caucasus" (awarded to AMB). Further support was provided by the Gfoeller Renaissance Foundation (USA) and "Areni-1 Cave" Scientific-Research Foundation (Armenia) and the Institute of Archaeology and Ethnography of the National Academy of Sciences of the Republic of Armenia (supported by the Higher Education and Science Committee, Republic of Armenia, under grant number 21AG-6A080). We would like to thank Dr. Laura Romero-Sánchez for producing Fig. 1 and Netanel Paz for making Fig. 3. This research benefited greatly from the discussion during our conference at the University of Castilla-La Mancha, Toledo, Spain, from the 19 to May 24, 2024. We are grateful for their hospitality. The authors sincerely thank the two anonymous reviewers, editor Donatella Magri, and guest editor Erella Hovers for their thoughtful and constructive comments, which greatly enhanced the quality of this manuscript. We extend special appreciation to Kharshatur Meliksetian for his invaluable support and positive evaluation of this research.

Appendix A. Supplementary data

Supplementary data to this article can be found online at <https://doi.org/10.1016/j.quascirev.2025.109623>.

Data availability

All data and/or code is contained within the submission.

References

- Adler, D.S., Wilkinson, K.N., Blockley, S., Mark, D.F., Pinhasi, R., Schmidt-Magee, B.A., Nahapetyan, S., Mallol, C., Berna, F., Glauberman, P.J., Raczyński-Henk, Y., Wales, N., Frahm, E., Jöris, O., MacLeod, A., Smith, V.C., Cullen, V.L., Gasparian, B., 2014. Early Levallois technology and the lower to Middle Paleolithic transition in the Southern Caucasus. *Science* 345, 1609–1613. <https://doi.org/10.1126/science.1256484>.
- Aitken, M.J., 1985. *Thermoluminescence Dating*. Academic Press, London.
- Allen, L.G., Gibbard, P.L., 1994. Pleistocene evolution of the Solent river of southern England. *Quat. Sci. Rev.* 12 (6), 503–528. [https://doi.org/10.1016/0277-3791\(93\)90067-V](https://doi.org/10.1016/0277-3791(93)90067-V).
- Alley, R.B., Ágústsdóttir, A.M., 2005. The 8k event: cause and consequences of a major Holocene abrupt climate change. *Quat. Sci. Rev.* 24 (10–11), 1123–1149. <https://doi.org/10.1016/j.quascirev.2004.12.004>.
- Antoine, P., 1994. The Somme Valley terrace system (northern France); a model of river response to Quaternary climatic variations since 800, 000 BP. *Terra Nova* 6, 453–464. <https://doi.org/10.1111/j.1365-3121.1994.tb00889.x>.
- Antoine, P., Lautridou, J.P., Laurent, M., 2000. Long-term fluvial archives in NW France: response of the seine and Somme rivers to tectonic movements, climatic variations and sea-level changes. *Geomorphology* 33, 183–207. [https://doi.org/10.1016/S0169-555X\(99\)00122-1](https://doi.org/10.1016/S0169-555X(99)00122-1).

- Antoine, P., Limondin-Lozouet, N., Lautridou, J.P., Sommè, J., 2004. Pleistocene fluvial terraces from northwestern France (Seine, Somme): synthesis, and prospects. *Quaternaire* 15 (1–2), 41–53. <https://doi.org/10.3406/quate.2004.1742>.
- Antoine, P., Coutard, S., Gibbard, P.L., Hallegouet, B., Lautridou, J.P., Ozouf, J.C., 2007. The Pleistocene rivers of the English Channel region. *J. Quat. Sci.* 18 (3–4), 227–243. <https://doi.org/10.1002/jqs.751>.
- Arakelyan, R.A., 1949. Schematic Geological Map South-East Armenia and surrounding part of Nakhichevan ASSR, 1:100.000 scale. Academy of Science of ASSR.
- Arimura, M., Petrosyan, A., Arakelyan, D., Nahapetyan, S., Gasparyan, B., 2018. A preliminary report on the 2015 and 2017 field seasons at the Lernagog-1 site in Armenia. ARAMAZD: Armenian Journal of Near Eastern Studies 12 (1), 1–19. <https://doi.org/10.32028/ajnes.v12i1.888>.
- Avagyan, A., Sosson, M., Sahakyan, L., Sheremet, Y., Vardanyan, S., Martirosyan, M., Muller, C., 2018. Tectonic evolution of the northern margin of the Cenozoic Ararat basin, Lesser Caucasus, Armenia. *J. Petrol. Geol.* 41 (4), 495–512. <https://doi.org/10.1111/jpg.12718>.
- Baksí, A.K., 2007. A quantitative tool for detecting alteration in undisturbed rocks and minerals-I: water, chemical weathering and atmospheric argon. *Geol. Soc. of Amer. Spec. Pap.* 285–303. [https://doi.org/10.1130/2007.2430\(15\)](https://doi.org/10.1130/2007.2430(15)).
- Bar Yosef, O., 1994. The lower Paleolithic of the Near East. *J. World PreHistory* 8 (3), 211–265.
- Benito-Calvo, A., Moreno, D., Fujioka, T., López, G.I., Martín-González, F., Martínez-Fernández, A., Hernando-Alonso, I., Karampaglidis, T., Bermúdez de Castro, J.M., Gutiérrez, F., 2022. Towards the steady state? A long-term river incision deceleration pattern during Pleistocene entrenched (Upper Ebro River, Northern Spain). *Global Planet. Change* 213, 103813. <https://doi.org/10.1016/j.gloplacha.2022.103813>.
- Björck, S., Kromer, B., Johnsen, S., Bennike, O., Hammarlund, D., Lemdahl, G., Possnert, G., Rasmussen, T.L., Wohlfarth, B., Hammer, C.U., Spurk, M., 1996. Synchronised terrestrial-atmospheric deglacial records around the North Atlantic. *Science* 274 (5290), 1155–1160. <https://doi.org/10.1126/science.274.5290.1155>.
- Boichenko, G., Cowgill, E., Godoladze, T., Stahl, T.A., Gogoladze, S., Merebashvili, G., Okrotsvaridze, A., Torres, R., Binnie, S., Ritter, B., 2025. Kura (Mtkvari) River terraces record fluvial response to the collision of the greater and lesser caucasus thrust belts, Georgia. *Geomorphology* 476, 109656. <https://doi.org/10.1016/j.geomorph.2025.109656>.
- Bøtter-Jensen, L., Andersen, C.E., Duller, G.A.T., Murray, A.S., 2003. Developments in radiation, stimulation and observation facilities in luminescence measurements. *Radiat. Meas.* 37, 535–541. [https://doi.org/10.1016/S1350-4487\(03\)00020-9](https://doi.org/10.1016/S1350-4487(03)00020-9).
- Brennan, B.J., Lyons, R.G., Phillips, S.W., 1991. Attenuation of alpha particle track dose for spherical grains. *Int. J. Radiat. Appl. Instrumentation. Part A* 18, 249–253. [https://doi.org/10.1016/1359-0189\(91\)90119-3](https://doi.org/10.1016/1359-0189(91)90119-3).
- Bridgland, D.R., 1994. Dating of Lower Palaeolithic industries within the framework of the Lower Thames terrace sequence. In: Ashton, N., David, A. (Eds.), *Stories in Stone. Lithic Studies Society Occasional Paper* 4, pp. 28–40. London.
- Bridgland, D.R., 2000. River terrace systems in north-west Europe: an archive of environmental change, uplift and early human occupation. *Quat. Sci. Rev.* 19, 1293–1303. [https://doi.org/10.1016/S0277-3791\(99\)00095-5](https://doi.org/10.1016/S0277-3791(99)00095-5).
- Bridgland, D.R., Westaway, R., 2008. Climatically controlled river terrace staircases: a worldwide Quaternary phenomenon. *Geomorphology* 98 (3–4), 285–315. <https://doi.org/10.1016/j.geomorph.2006.12.032>.
- Briqueu, L., Bougault, H., Joron, J.L., 1984. Quantification of Nb, Ta, Ti and V anomalies in magmas associated with subduction zones: petrogenetic implications. *Earth Planet. Sci. Lett.* 68, 297–308.
- Bull, W.B., 1977. *Tectonic Geomorphology of the Mojave Desert*, p. 188. California. Unpublished Technical Report for the U.S. Geological Survey, Contact no. 14-08-0001-G-394.
- Bull, W.B., 1991. Geomorphic responses to climatic change. *Prog. Phys. Geogr. Earth Environ.* 1 (2), 222–270. <https://doi.org/10.1177/030913337700100202>. Oxford University Press, New York, 326 pp. uvial-fan environment.
- Bunn, H., Harris, J.W.K., Isaac, G., Kaufulu, Z., Kroll, E., Schick, K., Toth, N., Behremsmeyer, A.K., 1980. FxJ50: an early Pleistocene site in northern Kenya. *World Archaeol.* 12, 109–136. <https://doi.org/10.1080/00438243.1980.9979787>.
- Carlson, A.E., 2010. What caused the Younger Dryas cold event? *Geology* 38 (4), 383–384. <https://doi.org/10.1130/focus042010.1>.
- Carrasco, R.M., Fernández-Lozano, J., Karampaglidis, T., Soteres, R.L., Braucher, R., Gairoard, S., Petrosyan, A., Nahapetyan, S., Arakelyan, D., Pedraza, J., Gasparyan, B., Aumaitre, G., Keddoudouche, K., Zaidi, F., 2025. Geomorphology, first ^{36}Cl datings and chrono-evolutionary model of Mount Aragats paleoglaciers (Armenia). *Quat. Sci. Rev.* 361, 109404. <https://doi.org/10.1016/j.quascirev.2025.109404>. ISSN 0277-3791.
- Chahoud, J., Vila, E., Balasescu, A., Crassard, R., 2016. The diversity of late Pleistocene and Holocene wild ungulates and kite structures in Armenia. *Quat. Int.* 395, 133–153. <https://doi.org/10.1016/j.quaint.2015.04.024>.
- Chernyshev, I.V., Lebedev, V.A., Arakelyants, M.M., Jrashyan, M.T., Gukasyan, Y.G., 2002. Quaternary geochronology of the Aragats volcanic center, Armenia: evidence from K-Ar dating. *Dokl. Earth Sci.* 384, 393–398.
- Cox, S.E., Hemming, S.R., Tootell, D., 2020. The Isotopx NGX and ATONA Faraday amplifiers. *Geochronology* 2, 231–243. <https://doi.org/10.5194/gchron-2-231-2020>.
- Crabtree, S.M., Lange, R.A., 2011. Complex phenocryst textures and zoning patterns in Andesites and Dacites: evidence of degassing-induced rapid crystallization? *J. Petrol.* 52 (1), 3–38. <https://doi.org/10.1093/petrology/egg067>.
- Cresswell, A.J., Carter, J., Sanderson, D.C.W., 2018. Dose rate conversion parameters: assessment of nuclear data. *Radiat. Meas.* 120, 195–201. <https://doi.org/10.1016/j.radmeas.2018.02.007>.
- Cunha, P., Martins, A., Huot, S., Murray, A., Raposo, L., 2008. Dating the Tejo River lower terraces (Rodão, Portugal) to assess the role of tectonics and uplift. *Geomorphology* 102 (1–2), 43–54.
- Djamali, M., de Beaulieu, J.L., Shah-hosseini, M., Andrieu-Ponel, V., Ponel, P., Amini, A., Akhani, H., Leroy, S.A.G., Stevens, L., Lahijani, H., Brewer, S., 2008. A late Pleistocene long pollen record from Lake Urmia, NW Iran. *Quaternary Research* 69, 413–420.
- Dunnell, R.C., 1992. The notion site. In: Rossignol, J., Wandsnider, L. (Eds.), *Space, Time, and Archaeological Landscapes*. Plenum, New York, pp. 21–41.
- Faure, G., Mensing, T.M., 1993. K-Ar dates and paleomagnetic evidence for Cretaceous alteration of Mesozoic basaltic lava flows, Mesa Range, northern Victoria Land, Antarctica. *Chem. Geol.* 109 (1–4).
- Fayvush, G.M., Aleksanyan, A.S., 2016. Habitats of Armenia. National Academy of Sciences of the Republic of Armenia. Institute of Botany, Yerevan, p. 360. ISBN: 978-9939-1-0347-1.
- Ferring, R., Oms, O., Agusti, J., Berna, F., Nioradze, M., Shelia, T., Tappan, M., Vekua, A., Zhvania, D., Lordkipanidze, D., 2011. Earliest Human Occupations at Dmanisi (Georgian Caucasus) Dated to 1.85–1.78 Ma, 108. Proceedings of the National Academy of Sciences, pp. 10432–10436. <https://doi.org/10.1073/pnas.1106638108>.
- Ferring, R., Oms, O., Nomade, S., Humphrey, J.D., Tappan, M., Coil, R., Shelia, T., Crislip, P., Chagelishvili, R., Kiladze, G., Guillou, H., Lordkipanidze, D., 2022. Early Pleistocene stratigraphy, sedimentary environments, and formation contexts at Dmanisi in the Georgian Caucasus. *J. Hum. Evol.* 172, 103254. <https://doi.org/10.1016/j.jhevol.2022.103254>.
- Foley, R., 1981a. A model of regional archaeological structure. *Proc. Prehist. Soc.* 47, 1–17.
- Foley, R., 1981b. Off-site archaeology: an alternative approach for the short-sited. In: Hodder, I., Isaac, G., Hammond, N. (Eds.), *Pattern of the Past: Studies in Honour of David Clarke*. Cambridge University Press, Cambridge, pp. 157–183.
- Ford, D.C., Williams, P.W., 2007. *Karst Hydrogeology and Geomorphology*. Wiley.
- Gabrielyan, A., Sarkisyan, H., Simonyan, G., 1981. *Seismotectonics of the Armenian SSR*. Yerevan University, Yerevan, 283pp (in Russian).
- Gasparyan, B., Petrosyan, A., Glauberman, P., Adigyozyalyan, A., Arimura, M., Frahm, E., Nahapetyan, S., Arakelyan, D., Sherriff, J., Karampaglidis, T., Krakovsky, M., Malinsky-Buller, A., 2023. Dalarik-1: a new lower Paleolithic Cave site in the Republic of Armenia. In: Grekyan, Y.H., Bobokhyan, A.A. (Eds.), Systemizing the past Papers in near Eastern and Caucasian Archaeology Dedicated to Pavel S. Avetisyan on the Occasion of His 65th Birthday. Archaeopress Archaeology, pp. 127–141. <https://doi.org/10.2307/jji.608099>.
- Geology of the Armenian SSR, 1962. *Geomorphology, Volume I*, Publishing House of the Academy of Sciences of the Armenian SSR, Yerevan, p. 582.
- Geology of the Armenian SSR, 1964. *Stratigraphy, Volume II*, Publishing House of the Academy of Sciences of the Armenian SSR, Yerevan, p. 432.
- Gevorgyan, H., Repstock, A., Schulz, B., Meliksetian, K., Breitkreuz, C., Israyelyan, A., 2018. Decoding a post-collisional multistage magma system: the Quaternary ignimbrites of Aragats stratovolcano, western Armenia. *Lithos* 318–319, 267–282. <https://doi.org/10.1016/j.lithos.2018.07.024>.
- Gevorgyan, H., Breitkreuz, C., Meliksetian, K., Israyelyan, A., Ghukasyan, Y., Pfänder, J. A., Sperner, B., Miggins, D.P., Koppers, A., 2020. Quaternary ring plain- and valley-confined pyroclastic deposits of Aragats stratovolcano (Lesser Caucasus): Lithofacies, geochronology and eruption history. *J. Volcanol. Geoth. Res.* 401, 106928. <https://doi.org/10.1016/j.volgeores.2020.106928>.
- Ghukasyan, Y., 1985. Petrography, mineralogical-geochemical Characteristics and the History of the Forming of Aragats Volcanic Complex. Phd Dissertation. IGS Academy of Sciences, Yerevan, Armenian SSR, p. 400.
- Gibbard, P.L., 1988. The history of the great northwest European rivers during the past 3 million years. *Phil. Trans. Biol. Sci.* 318 (1196), 559–602. <https://doi.org/10.1098/rstb.1988.0024>.
- Gibbard, P.L., Allen, L.G., 1994. Drainage evolution in south and east England during the Pleistocene. *Terra Nova* 6 (5), 444–452. <https://doi.org/10.1111/j.1365-3121.1994.tb00888.x>.
- Gibbard, P.L., Lewin, J., 2002. Climate and related controls on interglacial fluvial sedimentation in lowland Britain. *Sediment. Geol.* 151 (3–4), 187–210. [https://doi.org/10.1016/S0037-0738\(01\)00253-6](https://doi.org/10.1016/S0037-0738(01)00253-6).
- Glauberman, P., Gasparyan, B., Sherriff, J., Wilkinson, K., Li, B., Knul, M., Brittingham, A., Hren, M.T., Arakelyan, D., Nahapetyan, S., Raczyński-Henk, Y., Haydosyan, H., Adler, D.S., 2020. Barozh 12: formation processes of a late Middle Paleolithic open-air site in western Armenia. *Quat. Sci. Rev.* 236, 106276. <https://doi.org/10.1016/j.quascirev.2020.106276>.
- Guérin, G., Mercier, N., Adamiec, G., 2011. Dose-rate conversion factors: update. *Anc. TL* 29, 5–8.
- Guillou, H., Carracedo, J.C., Pérez Torrado, F.J., Rodríguez Badiola, E., 1996. K-Ar ages and magnetic stratigraphy of a hotspot-induced, fast grown oceanic island: El Hierro, Canary Islands. *J. Volc. Geoth. Res.* 73, 141–155.
- Guillou, H., Nomade, S., Carracedo, J.C., Kissel, C., Laj, C., Perez Torrado, F.J., Wandres, C., 2011. Effectiveness of combined unspiked K-Ar and 40Ar/39Ar dating methods in the ^{14}C age range. *Quat. Geoch.* 6, 530–538.
- Hay, R.L., 1976. *Geology of the Olduvai Gorge; a Study of Sedimentation in a Semiarid Basin*. University of California Press, Berkeley.
- Hovers, E., Ekshtain, R., Greenbaum, N., Malinsky-Buller, A., Nir, N., Yeshurun, R., 2014. Islands in a stream? Reconstructing site formation processes in the late Middle Paleolithic site of Ein Qashish, northern Israel. *Quat. Int.* 331. <https://doi.org/10.1016/j.quaint.2014.01.028>.

- Huntley, D.J., Lamothe, M., 2001. Ubiquity of anomalous fading in K-feldspars and the measurement and correction for it in optical dating. *Can. J. Earth Sci.* 38, 1093–1106. <https://doi.org/10.1139/cjes-38-7-1093>.
- Ikeda, S., Toriumi, M., Yoshida, H., Shimizu, I., 2002. Experimental study of the textural development of igneous rocks in the late stage of crystallization: the importance of interfacial energies under non-equilibrium conditions. *Contrib. Mineral. Petrol.* 142, 397–415.
- Innocenti, F., Kolios, N., Manetti, P., Rita, F., Villari, L., 1982. Acid and basic late Neogene volcanism in central Aegean Sea: its nature and geotectonic significance. *Bull. Volcanol.* 45, 87–97. <https://doi.org/10.1007/BF02600365>.
- Irvine, T.N., Baragar, W.R.A., 1971. A guide to chemical classification of the common volcanic rocks. *Can. J. Earth Sci.* 8, 523–548. <https://doi.org/10.1139/e71-055>.
- Jennings, J.N., 1985. *Karst Geomorphology*. Basil Blackwell.
- Joannin, S., Ali, A.A., Ollivier, V., Roiron, P., Peyron, O., Chevaux, S., Court-Picon, M., Chataigner, C., 2014. Vegetation, fire and climate history of the Lesser Caucasus: a new Holocene record from Zarishat fen (Armenia). *J. Quat. Sci.* 29 (1), 70–82.
- Karakhanyan, A., Jrbashyan, R., Trifonov, V., Philip, H., Arakelian, S., Avagyan, A., Baghdasaryan, H., Davtian, V., Ghoukasyan, Y., 2003. Volcanic hazards in the region of the Armenian Nuclear Power Plant. *J. Volcanol. Geotherm. Res.* 126, 31–62.
- Karakhanyan, A.S., Trifonov, V.G., Philip, H., Avagyan, A., Hessami, K., Jamali, F., Bayraktutan, M.S., Bagdassarian, H., Arakelian, S., Davtian, V., Adilkhanian, A., 2004. Active faulting and natural hazards in Armenia, eastern Turkey and northwestern Iran. *Tectonophysics* 380 (3e4), 189219.
- Jourdan, F., Renne, P., Reimold, W., 2009. An appraisal of the ages of terrestrial impact structures. *Earth and Planetary Science Letters* 286, 1–13. <https://doi.org/10.1016/j.epsl.2009.07.009>.
- Karakhanyan, A., Arakelyan, A., Avagyan, A., Sadoyan, T., 2016. Aspects of the seismotectonics of Armenia: new data and reanalysis. In: Sorkhabi, R. (Ed.), *Tectonic Evolution, Collision, and Seismicity of Southwest Asia: in Honor of Manuel Berberian's Forty Years of Research Contributions*, 525. Geological Society of America, Boulder, CO, USA, pp. 1–32.
- Karampaglidis, T., Benito-Calvo, A., Pérez-González, A., 2020. Understanding the Quaternary evolution of an intramountain staircase terraces model using morphometric indices: lozoya River, Central System, Spain. *Estud. Geol.* 76 (2), e134. <https://doi.org/10.3989/egeo.43508.527>.
- Karampaglidis, T., Fenn, K., Gasparyan, B., Braucher, R., Lauer, T., Vainer, S., Gevorgyan, H., Arakelyan, D., Oikonomou, I., Haydosyan, H., Rogall, D., Carrasco, R.M., Pedraza, J., Petrosyan, A., Malinsky-Buller, A., 2025. Paleolithic hominid occupations and Quaternary geomorphological evolution in the NE Ararat Depression (Armenia). *Quat. Sci. Rev.* 368, 109532. <https://doi.org/10.1016/j.quascirev.2025.109532>.
- Karapetian, S.G., Jrbashian, R.T., Mnatsakanian, A.K., 2001. Late collision rhyolitic volcanism in the northeastern part of the Armenian highland. *J. Volcanol. Geoth. Res.* 112, 189–220. [https://doi.org/10.1016/S0377-0273\(01\)00241-4](https://doi.org/10.1016/S0377-0273(01)00241-4).
- Keskin, M., 2003. Magma generation by slab steepening and breakoff beneath a subduction-accretion complex: an alternative model for collision-related volcanism in Eastern Anatolia, Turkey. *Geophys. Res. Lett.* 30, 1–4.
- Keskin, M., Pearce, J.A., Mitchell, J.G., 1998. Volcano-stratigraphy and geochemistry of collision-related volcanism on the Erzurum-Kars plateau, northeastern Turkey. *J. Volcanol. Geotherm. Res.* 85, 355–404. [https://doi.org/10.1016/S0377-0273\(98\)00063-8](https://doi.org/10.1016/S0377-0273(98)00063-8).
- Kirscher, U., Gevorgyan, H., Meliksetian, K., Navasardyan, G., Dallanave, E., Breitkreuz, C., Bachtadse, V., 2020. Pleistocene ignimbrites of western Armenia - paleomagnetic and magnetic anisotropy constraints on flow direction and stratigraphy. *J. Volcanol. Geoth. Res.* 402, 1–16. <https://doi.org/10.1016/j.jvolgeores.2020.106982>.
- Kobashi, T., Severinghaus, J.P., Brook, E.J., 2007. Precise timing and characterization of abrupt climate change during the Early Holocene. *Quat. Sci. Rev.* 26 (9–10), 1211–1222. <https://doi.org/10.1016/j.quascirev.2007.01.009>.
- Kolb, T., Tudyka, K., Kadereit, A., Lomax, J., Poręba, G., Zander, A., Zipf, L., Fuchs, M., 2022. The pdose system: determination of environmental dose rates by combined alpha and beta counting-performance tests and practical experiences. *Geochronology* 4, 1–31. <https://doi.org/10.5194/gchron-4-1-2022>.
- Koppers, A.A.P., 2002. ArAr CALC software for 40Ar/39Ar age calculations. *Comp. and Geosci.* 28, 605–619.
- Kreutzer, S., Schmidt, C., DeWitt, R., Fuchs, M., 2014. The a-value of polymimetal fine grain samples measured with the post-IR IRSL protocol. *Radiat. Meas.* 69, 18–29. <https://doi.org/10.1016/j.radmeas.2014.04.027>.
- Kuzucuoğlu, C., Christol, A., Mouralidis, D., Doğu, A.-F., Akköprü, E., Fort, M., Brunstein, D., Zorer, H., Fontugne, M., Karabiyikoğlu, M., Scaillet, S., Reyss, J.-L., Guillou, H., 2010. Formation of the Upper Pleistocene terraces of Lake Van (Turkey). *J. Quaternary Sci.* 25, 1124–1137. ISSN 0267-8179.
- Le Bas, M.J., Le Maître, R.W., Streckeisen, A., Zanettin, B., 1986. A chemical classification of volcanic rocks based on the total alkali-silica diagram. *J. Petrol.* 27, 745–750. <https://doi.org/10.1093/petrology/27.3.745>.
- Lebedev, V.A., Chernyshev, I.V., Yakushev, A.I., 2011. The initiation time and the duration of Quaternary magmatism in the Aragats neovolcanic area, Lesser Caucasus, Armenia. *Dokl. Earth Sci.* 437, 808e812.
- Lee, J.Y., Martí, K., Severinghaus, K., Kawamura, K., Yoo, H.S., Lee, J.B., Kim, J.S., 2006. A redetermination of the isotopic abundances of atmospheric Ar. *Geochim. Cosmochim. Acta* 70, 4507–4512.
- Liu, J.Q., Ren, Z.Y., Nichols, A.R.L., Song, M.S., Qian, S.P., Zhang, Y., Zhao, P.P., 2015. Petrogenesis of Late Cenozoic basalts from North Hainan Island: constraints from melt inclusions and their host olivines. *Geochim. Cosmochim. Acta* 152 (0), 89–121. <https://doi.org/10.1016/j.gca.2014.12.023>.
- Innocenti, F., Mazzuoli, R., Pasquare, G., Radicati di Brozolo, F., Villari, L., 1982. Tertiary and Quaternary volcanism of the Erzurum-Kars area (Eastern Turkey): geochronological data and geodynamic evolution. *J. Volcanol. Geotherm. Res.* 13, 223–240.
- Lynn, K.J., Shea, T., Garcia, M.O., 2017. Nickel variability in Hawaiian olivine: evaluating the relative contributions from mantle and crustal processes. *Am. Mineral.* 102, 507–518.
- Malinsky-Buller, A., Glauberman, P., Wilkinson, K., Li, B., Frahm, E., Gasparyan, B., Timms, R., Adler, D.S., Sherriff, J., 2020. Evidence for Middle Palaeolithic occupation and landscape change in central Armenia at the open-air site of Alapars-1. *Quat. Res.* 1–25. <https://doi.org/10.1017/qua.2020.61>.
- Malinsky-Buller, A., Hovers, E., Marder, O., 2011. Making time: “living floors”. “palimpsests” and site formation processes - A perspective from the open-air Lower Paleolithic site of Revadim Quarry, Israel. *Journal of Anthropological Archaeology* 30, 89–101. <https://doi.org/10.1016/j.jaa.2010.11.002>.
- Mania, D., 1995. The Zwischen interglacial complex and the Holsteinian in Central Germany. *Quat. Int.* 28, 17–20. [https://doi.org/10.1016/1040-6182\(95\)00041-0](https://doi.org/10.1016/1040-6182(95)00041-0).
- McDonough, W.F., Sun, S.-S., 1995. The composition of the Earth. *Chem. Geol.* 120, 223–253.
- Meliksetian, K., Savov, I., Connor, C., Halama, R., Jrbashyan, R., Navasardyan, G., Ghukasyan, Y., Gevorgyan, H., Manucharyan, D., Ishizuka, O., 2014. Aragats Stratovolcano in Armenia-volcano-stratigraphy and Petrology, vol. 567. EGU General Assembly Conference Abstracts.
- Meliksetian, K., Neill, I., Barfod, D.N., Milne, E.J.M., Waters, E.C., Navasardyan, G., Grigoryan, E., Olive, V., Odling, N., Karakhanyan, A., 2021. Pleistocene-Holocene volcanism at the Karkar geothermal prospect, Armenia. *Quat. Geochronol.* 66, 101201. <https://doi.org/10.1016/j.quageo.2021.101201>.
- Messenger, E., Lordkipanidze, D., Kvavadze, E., Ferring, C.R., Voinchet, P., 2010b. Palaeoenvironmental reconstruction of Dmanisi site (Georgia) based on palaeobotanical data. *Quat. Int.* 223–224, 20–27. <https://doi.org/10.1016/j.quaint.2009.12.016>.
- Messenger, E., Lebreton, V., Marquer, L., Russo-Ermoli, E., Orain, R., Renault-Miskovsky, J., Lordkipanidze, D., Despriée, J., Peretto, C., Arzarello, M., 2011a. Palaeoenvironments of early hominins in temperate and Mediterranean Eurasia: new palaeobotanical data from Palaeolithic key-sites and synchronous natural sequences. *Quat. Sci. Rev.* 30, 1439–1447.
- Messenger, E., Nomade, S., Voinchet, P., Ferring, R., Mgelandze, A., Guillou, H., Lordkipanidze, D., 2011b. $^{40}\text{Ar}/^{39}\text{Ar}$ dating and phytolith analysis of the Early Pleistocene sequence of Kvemo-Orozmani (Republic of Georgia): Chronological and palaeoecological implications for the hominin site of Dmanisi. *Quat. Sci. Rev.* 30, 3099–3108. <https://doi.org/10.1016/j.quascirev.2011.07.008>.
- Montgomery, D.R., 2004. Observations on the role of lithology in strath terrace formation and bedrock channel width. *Am. J. Sci.* 304, 454–476. <https://doi.org/10.2475/ajs.304.5.454>.
- Murray, A.S., Wintle, A.G., 2000. Luminescence dating of quartz using an improved single-aliquot regenerative-dose protocol. *Radiat. Meas.* 32, 57–73. [https://doi.org/10.1016/S1350-4487\(99\)00253-X](https://doi.org/10.1016/S1350-4487(99)00253-X).
- Nakhutrishvili, 2012. The Vegetation of Georgia (South Caucasus). <https://doi.org/10.1007/978-3-642-29915-5>.
- Neill, I., Meliksetian, K., Allen, M.B., Navasardyan, G., Kuiper, K., 2015. Petrogenesis of mafic collision zonemagmatism: the Armenian sector of the Turkish-Iranian plateau. *Chem. Geol.* 403, 24–41.
- Niespolo, E.M., Rutte, D., Deino, A.L., Renne, P.R., 2017. Intercalibration and age of the Alder Creek sanidine $^{40}\text{Ar}/^{39}\text{Ar}$ standard. *Quat. Geochronol.* 39, 205–213.
- Nikogosian, I.K., Bracco Gartner, A.J.J., Mason, P.R.D., van Hinsbergen, D.J.J., Kuiper, K., Kirscher, U., Matveev, S., Grigoryan, A., Grigoryan, E., Israyelyan, A., van Bergen, M.J., Koornneef, J.M., Wijibrans, J.R., Davies, G.R., Meliksetian, K., 2023. The South Armenian Block: gondwanan origin and Tethyan evolution in space and time. *Gondwana Res.* 121, 168–195.
- Nomade, S., Renne, P.R., Vogel, N., Deino, A.L., Sharp, W.D., Becker, T.A., Jaouni, A.R., Mundil, R., 2005. Alder creek sanidine (ACs-2): a quaternary $^{40}\text{Ar}/^{39}\text{Ar}$ dating standard tied to the Cobb mountain geomagnetic event. *Chem. Geol.* 218, 315–338.
- Nomade, S., Scao, V., Guillou, H., Messenger, E., Mgelandze, A., Voinchet, P., Renne, P.R., Courtin-Nomade, A., Bardintzeff, J.M., Ferring, R., Lordkipanidze, D., 2016. Addendum. *Quat. Int.* 395, 60. <https://doi.org/10.1016/j.quaint.2015.07.042>.
- Oikonomou, I.A.K., Karampaglidis, T., Fenn, K., Gur-Arieh, S., Nora, N., Sánchez-Romero, L., Rogall, D.L., Vettese, D., Gasparyan, B., Petrosyan, P., Malinsky-Buller, A., 2025. Unravelling the formation processes and depositional histories of the Middle Palaeolithic Ararat-1 Cave, Armenia: a multiscalar and multiproxy geoarchaeological approach. *Quat. Sci. Rev.* 361, 109405. <https://doi.org/10.1016/j.quascirev.2025.109405>. ISSN 0277-3791.
- Ollivier, V., Nahapetyan, S., Roiron, P., Gabrielyan, I., Gasparyan, B., Chataigner, C., Joannin, S., Cornée, J.-J., Guillou, H., Scaillet, S., Munch, P., Krijgsman, W., 2010. Quaternary volcano-lacustrine patterns and paleobotanical data in South Armenia. *Quat. Int.* 223–224, 312–326.
- Ollivier, V., Fontugne, M., Lyonnet, B., 2015. Geomorphic response and ^{14}C chronology of base level changes induced by late Quaternary Caspian Sea mobility (middle Kura Valley, Azerbaijan). *Geomorphology* 230, 109–124.
- Oron, M., Roskin, J., Avni, Y., Porat, N., Aladjem, E., Yegorov, D., Vardi, J., Hovers, E., 2023. A conceptual model of multi-scale formation processes of open-air Middle Paleolithic sites in the arid Negev desert, Israel. *Quaternary Research* 116, 162–180. <https://doi.org/10.1017/qua.2023.31>.
- Pearce, J.A., 1996. A users guide to basalt discrimination diagrams. In: Wyman, D.A. (Ed.), *Trace Element Geochemistry of Volcanic Rocks: Applications for Massive Sulphide Exploration*, vol. 12. Geological Association of Canada Short Course Notes, pp. 79–113.

- Pearce, J.A., Bender, J.F., De Long, S.E., Kidd, W.S.F., Low, P.J., Guner, Y., Saroglu, F., Yilmaz, Y., Moorbath, S., Mitchell, J.G., 1990. Genesis of collision volcanism in eastern Anatolia, Turkey. *J. Volcanol. Geotherm. Res.* 44, 189–229.
- Peccerillo, R., Taylor, S.R., 1976. Geochemistry of Eocene calc-alkaline volcanic rocks from the Kastamonu area, northern Turkey. *Contrib. Mineral. Petrol.* 58, 63–81.
- Philip, H., Cisternas, A., Gvishiani, A., Gorshkov, A., 1989. The Caucasus: an actual example of the initial stages of continental collision. *Tectonophysics* 161, 1–21. [https://doi.org/10.1016/0040-1951\(89\)90297-7](https://doi.org/10.1016/0040-1951(89)90297-7).
- Philip, H., Avagyan, A., Karakhanian, A., Ritz, J.F., Rebai, S., 2001. Estimating slip rates and recurrence intervals for strong earthquakes along an intracontinental fault: example of the PamhakeSevaneSunik fault (Armenia). *Tectonophysics* 343 (3e4), 205e232.
- Pickarski, N., Litt, T., 2017. A new high-resolution pollen sequence at Lake Van, Turkey: insights into penultimate interglacial-glacial climate change on vegetation history. *Clim. Past* 13, 689–710.
- Pickarski, N., Kwiecien, O., Djamali, M., Litt, T., 2015. Vegetation and environmental changes during the last interglacial in eastern Anatolia (Turkey): a new high-resolution pollen record from Lake Van. *Palaeogeogr. Palaeoclimatol. Palaeoecol.* 431 (1), 145–158.
- Pope, M., Blundell, L., Scott, B., Cutler, H., 2016. Behaviour and process in the formation of the North European Acheulean record: towards a Unified Paleolithic Landscape approach. *Quat. Int.* 411, 85–94. <https://doi.org/10.1016/j.quaint.2016.01.070>.
- Potts, R., 1996. Evolution and climate variability. *Science* 273, 922–923.
- Potts, R., 2013. Hominin evolution in settings of strong environmental variability. *Quat. Sci. Rev.* 73, 1–13. <https://doi.org/10.1016/j.quascirev.2013.04.003>.
- Potts, R., Behrensmeyer, A.K., Ditchfield, P., 1999. Paleolandscape variation and Early Pleistocene hominid activities: members 1 and 7, Olorgesailie Formation, Kenya. *J. Hum. Evol.* 37, 747–788. <https://doi.org/10.1006/jhev.1999.0344>.
- Prescott, J.R., Hutton, J.T., 1994. Cosmic ray contributions to dose rates for luminescence and ESR dating: large depths and long-term time variations. *Radiat. Meas.* 23, 497–500. [https://doi.org/10.1016/1350-4487\(94\)90086-8](https://doi.org/10.1016/1350-4487(94)90086-8).
- Rasmussen, S.O., Andersen, K.K., Svensson, A.M., Steffensen, J.P., Vinther, B.M., Clausen, H.B., Andersen, M.L., Johnsen, S.J., Larsen, L.B., Bigler, M., Röthlisberger, R., Fischer, H., Goto-Azuma, K., Hansson, M.E., Ruth, U., 2006. A new Greenland ice core chronology for the last glacial termination. *J. Geophys. Res. Atmos.* 111 (D6). <https://doi.org/10.1029/2005JD006079>.
- Rebäi, S., Philip, H., Dobrath, L., Borisoff, B., Haessler, H., Cisternas, A., 1993. Active tectonics in the Lesser Caucasus: coexistence of compressive and extensional structures. *Tectonics* 12 (5), 1089–1114. <https://doi.org/10.1029/93TC00514>.
- Renjith, M.L., 2014. Micro-textures in plagioclase from 1994–1995 eruption, Barren Island Volcano: evidence of dynamic magma plumbing system in the Andaman subduction zone. *Geosci. Front.* 6 (1), 113–126.
- P.R., Balco, G., Ludwig, K.R., Mundil, R., Min, K., 2010. Response to the comment by W. H. Schwarz et al. on “Joint determination of 40K decay constants and 40Ar*/40K for the Fish Canyon sanidine standard, and improved accuracy for 40Ar/39Ar geochronology” by P.R. Renne et al. *Geoch. Cosm. Acta* 75, 5097–5100. <https://doi.org/10.1016/j.gca.2011.06.021>.
- Sayadyan, Y.V., 2006. Geology, Stratigraphy, and Paleogeography of the Upper Miocene, Pliocene, and Quaternary Periods of Armenia. Abstract of the Phd Dissertation, Moscow, 47pp (in Russian).
- Sayadyan, Y.V., 2009. Recent Geological History of Armenia. Pub. House “Gitutyun”, NAS RA. Yerevan, 357pp (in Russian).
- Schaen, A.J., Jicha, B.R., Hodges, K.V., Vermeesch, P., Stelten, M.E., Mercer, C.M., Phillips, D., Rivera, T.A., Jourdan, F., Matchan, E.L., Heming, S.R., Morgan, L.E., Kelley, S.P., Cassata, W.S., Heizler, M.T., Vasconcelos, P.M., Benowitz, J.A., Koppers, A.A.P., Mark, D.F., Niespolo, E.M., Sprain, C.J., Hames, W.E., Kuiper, K.F., Turpin, B.D., Renne, P.R., Ross, J., Nomade, S., Guillou, H., Webb, L.E., Cohen, B.A., Calvert, A.T., Joyce, N., Ganerød, M., Wijibrans, J., Ishizuka, O., He, H., Ramirez, A., Pfänder, J.A., Lopez-Martinez, M., Qiu, H., Singer, B.S., 2021. Interpreting and reporting $^{40}\text{Ar}/^{39}\text{Ar}$ geochronologic data. *Bull. Geol. Soc. Amer.* 133, 461–487.
- Schanz, S.A., Montgomery, D.R., 2016. Lithologic controls on valley width and strath terrace formation. *Geomorphology* 258, 58–68. <https://doi.org/10.1016/j.geomorph.2016.01.015>.
- Schwarzer, J., Stauffer, B., 1984. Age difference between polar ice and the air trapped in its bubbles. *Nature* 311 (5981), 45–47. <https://doi.org/10.1038/311045a0>.
- Schweizer, G., 1975. Untersuchungen Zur Physiogeographie Von Ostanatolien Und Nordwestiran. Geomorphologische, klima- Und Hydrogeographische Studien Im Vansee- Und Rezaiyehsee-Gebiet. Tübiner Geographische Studien, Institute of Geography, University of Tübingen.
- Severinghaus, J.P., Brook, E.J., 1999. Abrupt climate change at the end of the last glacial period inferred from trapped air in polar ice. *Science* 286 (5441), 930–934. <https://doi.org/10.1126/science.286.5441.930>.
- Sherriff, J.E., Wilkinson, K.N., Adler, D.S., Arakelyan, D., Beverly, E.J., Blockley, S.P.E., Gasparyan, B., Mark, D.F., Meliksetyan, K., Nahapetyan, S., Preece, K.J., Timms, R.G., 2019. Pleistocene volcanism and the geomorphological record of the Hrazdan valley, central Armenia: linking landscape dynamics and the Paleolithic record. *Quat. Sci. Rev.* 226, 105994. <https://doi.org/10.1016/j.quascirev.2019.105994>.
- Sherriff, J.E., Wilkinson, K.N., Harding, P., Hawkins, H., Timms, R.G.O., Adler, D.S., Beverly, E.J., Blockley, S.P.E., Gasparyan, B., Manning, C.J., Mark, D., Nahapetyan, S., Preece, K.J., 2022. Middle Pleistocene environments, landscapes and tephrostratigraphy of the Armenian highlands: evidence from Bird Farm 1, Hrazdan Valley. *J. Quat. Sci.* 37, 6–27. <https://doi.org/10.1002/jqs.3370>.
- Silva, P.G., Roquero, E., López-Recio, M., Huerta, P., Martínez-Grana, A.M., 2017. Chronology of fluvial terrace sequences for large Atlantic rivers in the Iberian Peninsula (Upper Tagus and Duero drainage basins, Central Spain). *Quat. Sci. Rev.* 1–17. <https://doi.org/10.1016/j.quascirev.2017.06.013>.
- Stokes, M., Mather, A.E., 2000. Response of Plio-Pleistocene alluvial systems to tectonically induced base-level changes, Vera Basin, SE Spain. *J. Geol. Soc.* 157 (2), 303–316.
- Stokes, M., Mather, A.E., Belfoul, M.A., 2017. Active folding and fluvial incision in the Moroccan High Atlas Mountains. *J. Geophys. Res.: Earth Surf.* 122 (6), 1236–1262. <https://doi.org/10.1002/2016JF004113>.
- Stuiver, M., Grootes, P.M., Braziunas, T.F., 1995. The GISP2 δ18O climate record of the past 16,500 years and the role of the sun, ocean, and volcanoes. *Quaternary Research* 44 (3), 341–354. <https://doi.org/10.1006/qres.1995.1079>.
- Sugden, P., Meliksetyan, K., Savov, I.P., Barfod, D., Wilson, M., Connor, C., Navasardyan, G., Grigoryan, E., Manucharyan, D., 2021. Post-collisional shift from polygenetic to monogenetic volcanism revealed by new $^{40}\text{Ar}/^{39}\text{Ar}$ ages in the southern Lesser Caucasus (Armenia). *J. Volcanol. Geotherm. Res.* 412, 107192. <https://doi.org/10.1016/j.jvolgeores.2021.107192>.
- Sun, S.-S., McDonough, W.F., 1989. Chemical and isotopic systematics of oceanic basalts: implications for mantle composition and processes. In: Saunders, A.D., Norry, M.J. (Eds.), *Magmatism in the Ocean Basins*, vol. 42. Geological Society of London Special Publication, pp. 313–345.
- Sweeting, M.M., 1973. *Karst Landforms*. Columbia University Press.
- Thordarson, T., Self, S., 1993. The Laki (skafárt fires) and Grýmsvötn eruptions in 1783–1785. *Bull. Volcanol.* 55, 233–263.
- Thordarson, T., Self, S., Oskarsson, N., Hulsebosch, T., 1996. Sulfur, chlorine, and fluorine degassing and atmospheric loading by the 1783–1784 AD Laki (Skaftafires) eruption in Iceland. *Bull. Volcanol.* 58, 205–225.
- Tudyka, K., Bluszcz, A., Poręba, G., Młosz, S., Adamiec, G., Kolarszky, A., Kolb, T., Lomax, J., Fuchs, M., 2020. Increased dose rate precision in combined α and β counting in the μ Dose system - a probabilistic approach to data analysis. *Radiat. Meas.* 134. <https://doi.org/10.1016/j.radmeas.2020.106310>.
- Tudyka, K., Koruszwic, M., Osadnik, R., Adamiec, G., Moska, P., Szymbak, A., Bluszcz, A., Zhang, J., Kolb, T., Poręba, G., 2023. μ Rate: an online dose rate calculator for trapped charge dating. *Archaeometry* 65, 423–443. <https://doi.org/10.1111/arcm.12828>.
- Van den Berg, M.W., Van Hoof, T.A.M., 2001. The Maas terrace sequence at Maastricht, southern Netherlands. *Neth. J. Geosci.* 80 (1), 51–65. <https://doi.org/10.1017/S0016774600022310>.
- Vandenbergh, J., 2008. The fluvial cycle at cold-warm-cold transitions in lowland regions: a refinement of theory. *Geomorphology* 98 (3–4), 275–284. <https://doi.org/10.1016/j.geomorph.2006.12.031>.
- von Suchodoletz, H., Gärtner, A., Hoth, S., Umlauft, J., Sukhishvili, L., Faust, D., 2016. Late pleistocene river migrations in response to thrust belt advance and sediment-flux steering - the Kura River (southern Caucasus). *Geomorphology*, 2016 266, 53–65.
- Westaway, R., Bridgland, D.R., Sinha, R., 2009. Fluvial sequences as evidence for landscape and climatic evolution in the Late Cenozoic: a synthesis of data from IGCP 518. *Global Planet. Change* 68 (4), 237–253. <https://doi.org/10.1016/j.gloplacha.2009.04.005>.
- White, W.B., 1988. *Geomorphology and Hydrology of Karst Terrains*. Oxford University Press.
- Whitney, D.L., Evans, B.W., 2010. Abbreviations for names of rock-forming minerals. *American Mineralogist* 95 (1), 185–187. <https://doi.org/10.2138/am.2010.3371>.
- Wolf, D., Faust, D., 2015. Fluvial terraces as archives of climate and tectonic activity: a review. *Quat. Sci. Rev.* 114, 203–226. <https://doi.org/10.1016/j.quascirev.2015.02.018>.
- Wolf, D., Lomax, J., Sahakyan, L., Hovakimyan, H., Profe, J., Schulte, P., von Suchodoletz, H., Richter, C., Hambach, U., Fuchs, M., Faust, D., 2022. Last glacial loess dynamics in the Southern Caucasus (NE-Armenia) and the phenomenon of missing loess deposition during MIS-2. *Sci. Rep.* 12 (1), 13269. <https://doi.org/10.1038/s41598-022-17021-5>.
- Meliksetyan, Kh., 2012. Geochemistry of volcanic series of Aragats region. *Natl. Acad. Sci. Inst. Geol. Sci.* 3, 34–59 (in Russian).